Design, Modeling, and Testing of a Novel Inductor for Electric Vehicles: Iron Nitride Soft
Magnetic Composites

A Senior Project
presented to
the Faculty of the Materials Engineering Department
California Polytechnic State University, San Luis Obispo

In Partial Fulfillment
of the Requirements for the Degree
Bachelor of Science

By

Sydney Fultz-Waters, Jacob Krynock

June, 2023

Table of Contents

List of Figures

List of Tables

Abstract

New technology for electric vehicles (EVs) must meet the requirements of higher energy usage, lower costs, and more sustainable source materials. One promising material for EV power system components is iron nitride (IN) soft magnetic composites (SMCs) because of their competitive magnetic properties and high abundance of the source materials. As part of an ongoing program at Sandia National Laboratories, this project focused on using computer modeling to optimize the prototyping process for an iron nitride SMC toroidal inductor to reach a target inductance of 600 µH. Four inductors with different combinations of wiring (26 AWG and 20 AWG) and vol% loading of iron nitride (65 vol% and 50 vol%) were fabricated at Cal Poly and characterized using an LCR meter. These inductors were also modeled using COMSOL Multiphysics™ with the Magnetic Fields module. The inductance data from the experiment and the model show that the 65 vol% IN prototypes and models agree with about 8% difference, while the 50 vol% IN samples show about a 9% difference between the prototype and the model. These results suggest that the model can predict inductance with both accuracy and precision with low confidence for the given sample size of four. An additional parameter of AC resistance is studied but the AC resistance results from the inductors and from the model generally do not agree closely, suggesting that the current model used in the project does not fully capture the mechanisms behind AC resistance of the inductor. With the focus of the project on inductance, the percent difference results of less than 9% across the four inductors that were tested increases confidence in the model's predictive capabilities for inductance only. Using the inductance results from both the model and experiment, the final suggested inductor design is a 65 vol% core with 150 windings of 20 AWG wire that is 8 cm across and 1.5 cm tall to reach the inductance goal of 600 µH based on analysis using the optimized COMSOL™ model.

1. Introduction

Electric vehicles (EVs) are quickly becoming more common as the technology behind them improves. According to a September 2022 tracking report by the International Energy Agency (IEA)[1], EV sales have risen substantially across the world since 2016 as illustrated in Figure 1. In the United States alone, the share of electric car sales rose from 1% in 2016 to 5% in 2021[1], shown by the green dot near the tops of the bars in Figure 1.
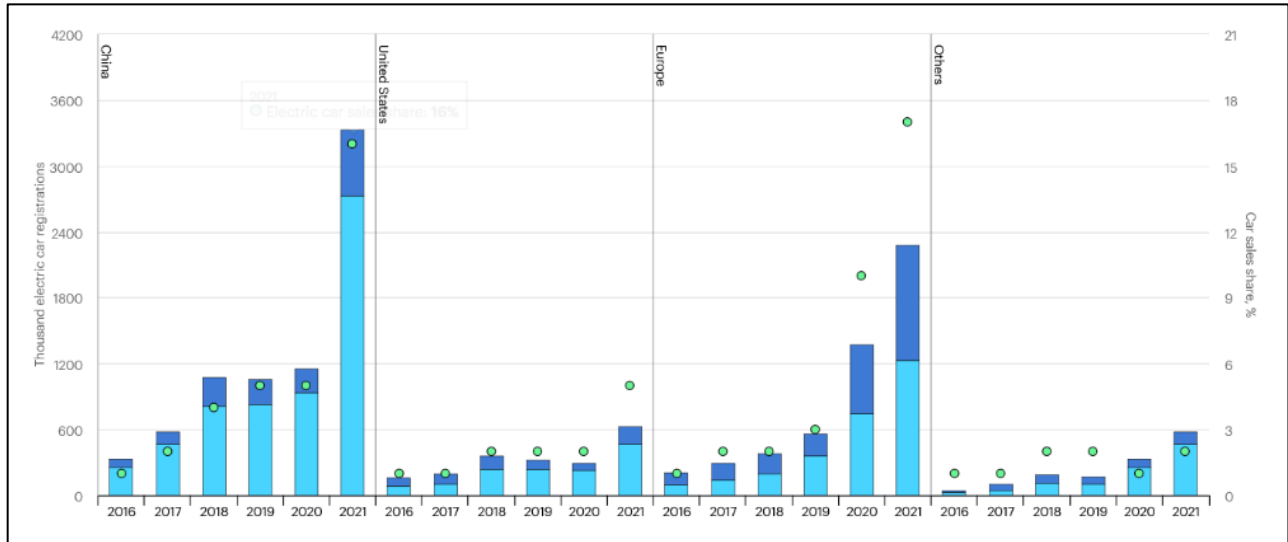
Figure 1. The number of electric vehicle registrations and sales across the world continues to grow over the years. The light shade in the chart represents the fully electric vehicles (battery EVs) while the dark shade represents the hybrid electric vehicles (plug-in hybrid EVs)[1].

As EVs continue to develop, existing requirements become harder to meet; longer travel means higher energy usage (more kW-h) without raising the cost. In addition to these two requirements, EV developers must also meet increased sustainability requirements. Current EVs rely heavily on critical metals such as lithium, nickel, and cobalt which come with supply issues as well as health and ethical concerns[1]. A solution to these issues is the development of new high power, low cost, sustainable materials across the board.

Although much of the focus for EV innovation is on increasing the energy density of batteries, other power components must also meet the above requirements. This project addresses a frequently overlooked component within all power systems: an inductor for voltage conversion, current smoothing, and more. Inductors in EV systems typically utilize a ferrite or laminated steel core, which can generate large power losses at high frequencies[2]. A promising alternative material

is iron-based soft magnetic composites (SMCs) because of their competitive magnetic properties and high abundance. The field of study of SMCs is quite broad, so this project focuses on current work at Sandia National Laboratories (Sandia) in Albuquerque, NM. In conjunction with our project sponsor at Sandia, we are building upon an existing iron nitride composite inductor to develop the optimal design to meet the high-power, low-cost requirements set by the Department of Energy (DoE) for EV power systems.

Currently, the iron nitride composite inductor is in the prototyping stage, which includes the fabrication of a complete sample followed by inductance testing to compare its inductance to the 600 µH inductance requirement set by a Sandia power converter design. Prior to the start of this project, the design of the inductor changed from a bobbin-style inductor to a toroid, which requires all new sizing, number of windings, and fabrication materials. Following the need for a new prototype design, our project problem statement is: *What is the optimal size, number of windings, vol% loading of iron nitride, and wire gauge to meet the 600 µH inductance requirement of the inductor?*

With limited facilities on the Cal Poly San Luis Obispo campus compared to Sandia, we are approaching the problem statement in a unique way: computer modeling and validation. Rather than making numerous prototypes to test different designs, we used the COMSOL™ Multiphysics software package to optimize the design of the inductor through computer modeling and fabricated the optimized inductor design to validate the model with real-life data from testing. The end goal of the project is a parametrized COMSOL™ model of the toroid that can accurately predict inductance to aid in the prototyping process for our sponsor at Sandia. The dual nature of the project is illustrated by the finite element analysis of the toroid next to the fabricated toroid in Figure 2.
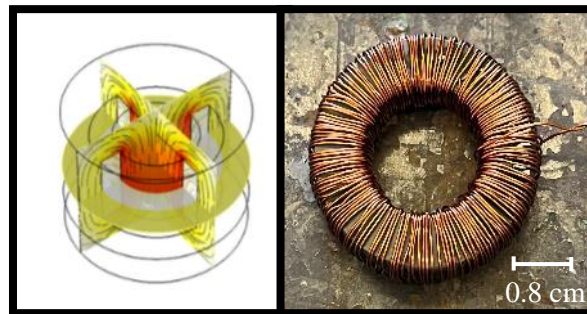
Figure 2. (Left) The optimized inductor design in COMSOL™, and (right) after fabrication.

2. Background

2.1. Introduction to Inductors

An inductor is a common component in electric circuits which stores energy in the form of a magnetic field [3]. As described by Maxwell's laws in 1865, a changing electric field will induce a magnetic field in accordance with the right-hand rule[4]. Therefore, an inductor achieves a directional magnetic flux by flowing AC (a changing electric field) through a coiled wire. This unique ability to contain and control magnetic flux through inductors has become exceptionally important in a wide array of electrical applications such as transformers, motors, generators, and power converters[5].

2.1.1. Applications of Inductors in Electric Vehicles

In general, inductors are used wherever current needs to be controlled, smoothed, or modified. Since an inductor acts as both a source and a load, it can be used to filter out certain frequencies of AC, convert high DC to low DC, or even convert AC to DC. In EVs, inductors are often used in DC/DC and AC/DC converters to control voltage and current to and from the battery by stepping the voltage up or down[6,7]. Typical converters utilize multiple inductors to provide a continuous power supply to the EV battery as shown in Figure 3. The inductance of the component determines the capacity and operation limits of the converter, so it is beneficial to maximize the inductance per volume[7]. In addition to the inductance requirement, inductors in EVs must be extremely reliable to withstand long-term use in automobiles while also remaining relatively inexpensive and miniaturized to avoid increasing EV costs further[6]. One element of this reliability includes the capacity to withstand high operating temperatures and vibrational loads[7]. Further research is needed to determine the specific operating temperatures and vibrations experienced by inductors in EV applications.
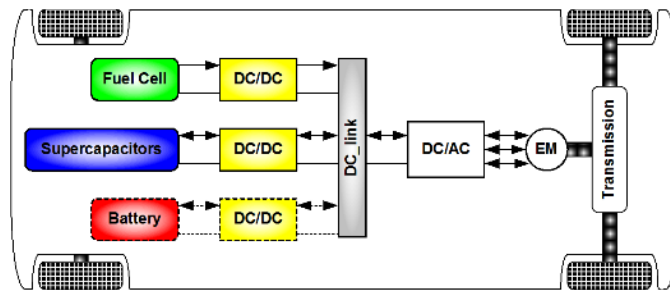
Figure 3. DC/DC and AC/DC converters have applications throughout the electric vehicle system, including adjusting voltage for the vehicle powertrain[8].

2.1.2. Characteristics of Toroidal Inductors

A high-performance inductor typically has two main parts: a highly electrically conductive copper winding and a highly permeable ferromagnetic core[3]. This project deals specifically with toroidal inductors, an example of which is shown in Figure 4 where h represents the height, a is the inner radius, and b is the outer radius. The variable r is the radial distance from the center to the midpoint of the toroid, or $0.5\ (b - a)$, and dr is a differential change in radial distance, while I is the current traveling through the inductor coil. When an AC source passes current through the copper windings, a magnetic field is induced in the rectangular cross section of the toroid. The ferromagnetic core, typically made of laminated iron or ferrite, effectively amplifies the strength of the magnetic field and leads to higher inductance values[9].
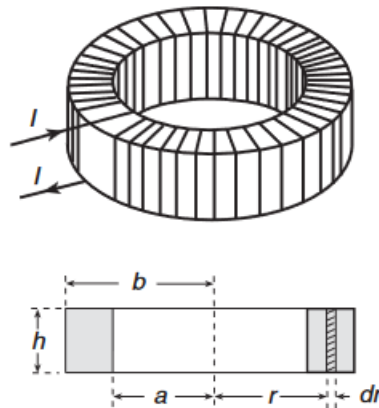
Figure 4. A toroidal inductor has a magnetic core in a donut shape with rectangular cross section and closely wound coils to improve performance[9].

The toroidal shape is chosen for a several reasons: it is relatively easily fabricated and it almost perfectly contains magnetic flux inside the windings, which minimizes signal distortion and electromagnetic interference (EMI) to adjacent components[10]. Therefore, the efficiencies of toroidal inductors are relatively high, so power losses can be attributed almost completely to copper losses in the winding and core losses in the ferromagnetic core[11]. To understand where these core losses come from, it's important to understand the basic properties of ferromagnetic materials.

2.1.3. Material Selection for Inductor Cores

As automotive and other industries aim for higher power, higher frequency, and more compact electronic devices, the demand for improved magnetic materials has followed. Magnetic materials

play a critical role in many AC applications including power transformers, electric motors, ignition coil cores, and other forms of inductor-based devices[12]. Energy loss within the magnetic cores can be attributed to three sources: hysteresis loss, eddy current loss, and magnetostriction effects[13]. These overall losses are collectively defined as the core loss.

Magnetic materials for inductor cores must satisfy the following requirements: high permeability and saturation magnetizations; low eddy current loss, hysteresis loss, and magnetostriction; reliable high temperature performance; scalability; and affordability[2].

2.2.   Overview of Ferromagnetic Materials

Ferromagnetic materials are a class of materials with the ability to be "permanently magnetized" due to the alignment of magnetic dipole domains within the bulk of the material. These magnetic domains are microscopic regions within the material where there is a long-range ordering of parallel electron spins[14]. A ferromagnetic material is considered unmagnetized if these magnetic domains are randomly oriented like in the left diagram of Figure 5. Applying a magnetic field to the material causes the magnetic domains to align themselves parallel to the direction of the externally applied field, allowing the material to generate a magnetic field of its own as shown in the diagram on the right in Figure 5.
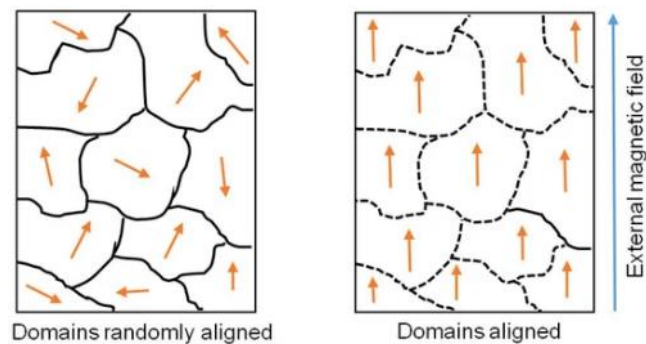
Figure 5. (Left) Magnetic domains in an unmagnetized ferromagnetic material. (Right) Magnetic domains align themselves in ferromagnetic materials when experiencing an external magnetic field[15].

A characteristic of ferromagnetic materials is their ability to stay magnetized to some degree after removing an external magnetic field, thus allowing them to function as permanent magnets. This tendency for these materials to "remember their magnetic history" is referred to as hysteresis[14].

2.2.1. Hysteresis Loss

The cycling between full magnetization, demagnetization, and full reverse magnetization in ferromagnetic materials is modeled by the hysteresis loop, an example of which is shown in Figure 6. Beginning with an unmagnetized material and increasing the magnitude of the externally applied magnetic field (H) will continue to align magnetic domains until full saturation magnetization (M_s), the point where all domains are parallel. When the external field decreases, only a fraction of domains relax back to non-parallel orientations. The degree to which domains stay parallel when the external field is dropped to zero is known as its remanence (M_r) [16] and is depicted as the y-intercept of the hysteresis loop in Figure 6. The x-intercept of the hysteresis loop in Figure 6 represents the strength of the magnetic field necessary to demagnetize a material and is defined as its coercivity (H_c) [16].
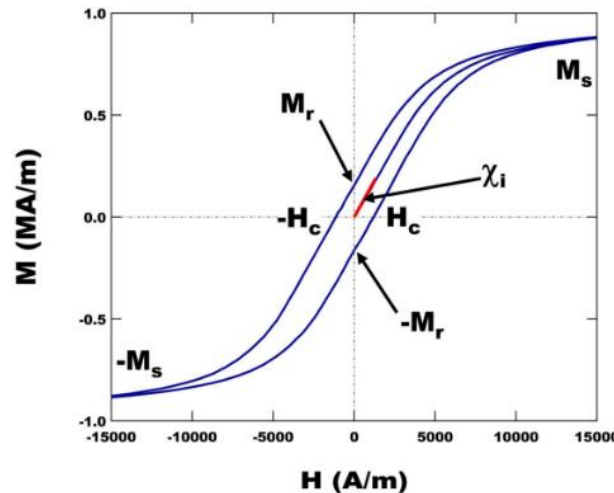
Figure 6. A hysteresis loop maps magnetization (M) as a function of the strength of an externally applied magnetic field (H) [17].

Increasing the magnitude of the applied field further in the negative direction will fully saturate the domains in the opposite direction. The area of the hysteresis loop is dependent upon a material's coercivity and remanence values, and a large area correlates to a large amount of energy dissipated as heat upon reversal of the applied magnetic field[14]. Hysteresis loss is simply a measure of power lost due to cycling a magnetic material with finite coercivity. Hysteresis curves can also help us identify whether the magnet is hard or soft.

2.2.2. Hard versus Soft Magnets and the Importance of Permeability

A hard magnet has a hysteresis curve like that on the left of Figure 7 and is defined as a ferromagnetic material that is difficult to magnetize and demagnetize. Conversely, a soft magnet is characterized by a hysteresis curve like that on the right of Figure 7 and is associated with very low coercivity values, and easy magnetization/ demagnetization. Soft magnetic materials are desirable in AC applications due to their low hysteresis loss shown by the narrow hysteresis curve on the right in Figure 7.
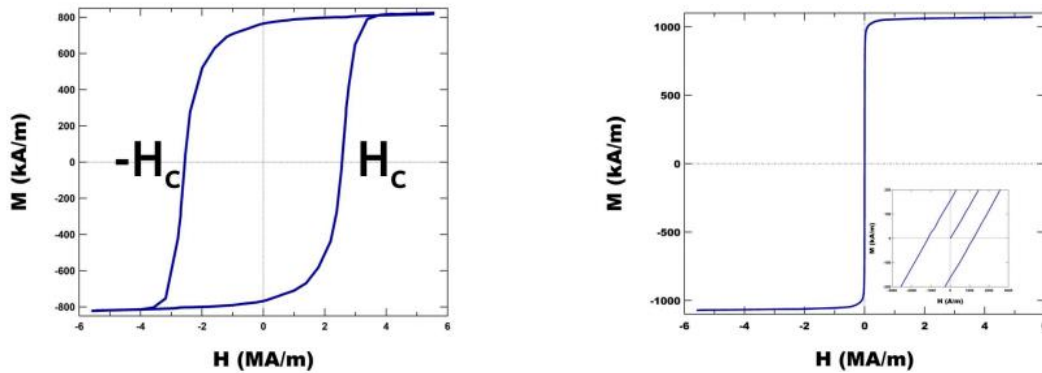
Figure 7. Comparison of hysteresis loops for hard vs soft magnets. (Left) A wide loop corresponds to a material with a high coercivity and low permeability (hard magnet). (Right) A narrow loop corresponds to a material with a low coercivity and typically high permeability (soft magnet) [2].

The extent to which the internally generated magnetic field multiplies the strength of the external field is known as magnetic susceptibility (χ), which is equal to the magnetization (M) divided by the magnetic field intensity (H) as described in Equation 2.1. The magnetic susceptibility is directly related to the material's relative permeability (μ_r) via Equation 2.2.

$$\chi = M/H \hspace{4cm} \text{Equation 2.1}$$

$$\mu_r = \chi + 1 \hspace{4cm} \text{Equation 2.2}$$

The easier it is to magnetize a material, the more permeable it is. Visually, the permeability is the slope of the hysteresis curve because typically $\chi \gg 1$ in ferromagnetic materials. Therefore, applications needing high permeability and low coercivity are satisfied with soft magnets because they require less current to achieve full saturation magnetization (M_s) [18].

2.2.3. Eddy Current Loss

Beyond permeability, another important parameter for inductor material selection is the eddy current losses. When an alternating magnetic field is induced within a ferromagnetic material, Faraday's law predicts that loops of current will be induced in planes perpendicular to the magnetic field as illustrated in Figure 8a[9,19]. These closed loops of current are known as eddy currents and dissipate power in the form of heat within the magnetic material[9,19]. The magnitude of eddy currents are proportional to the strength of the magnetic field, the area of the loop, the rate of change of magnetic flux, and the electrical conductivity of the material[20]. Therefore, by restricting the currents to circulate in small cross-sectional areas, eddy current losses can be reduced. Many inductor cores employ this tactic by making thin sections of ferritic material with electrically insulating coatings that are laminated together as in Figure 8b[19]. Choosing a more electrically resistive material is another tactic for reducing eddy current losses in inductor cores[9]. With this solution, it is important to choose a material that has high thermal stability.
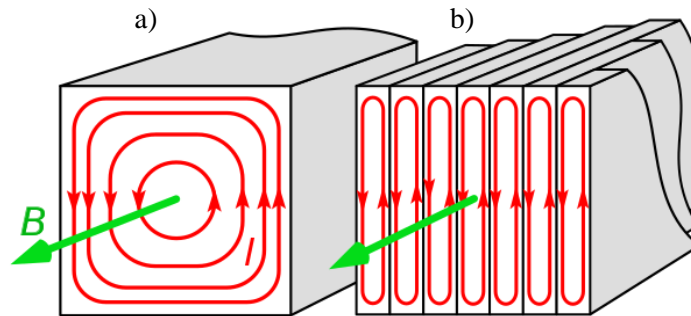
Figure 8. Eddy currents i_{ed} travel perpendicular to the magnetic field B in the core material of an inductor for both (a) bulk homogeneous materials and (b) laminated cores[21].

2.2.4. Magnetostriction

Another material property to consider for inductors is magnetostriction. Magnetostriction is an effect observed in all ferromagnetic materials where the magnetization and demagnetization of the material like that in Figure 9 causes small mechanical deformations in the crystal structure[22]. When the magnetic domains within the material are forced to align under an external magnetic field, the material's dimensions are strained in an orientation that minimizes the Gibbs free energy. When the material's magnetization is cycled under an AC frequency, a corresponding frequency of microscopic straining generates a vibration, dissipating energy in the form of heat and sound.

Although this energy loss is typically less significant than eddy current loss and hysteresis loss, it is a loss that should be accounted for, and is a property intrinsic to the material.
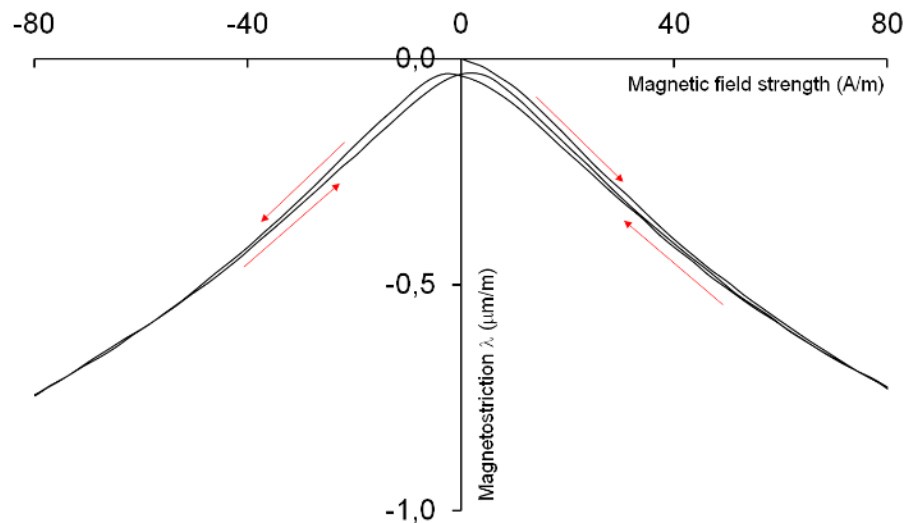
Figure 9. A hysteresis curve for magnetostriction shows a small amount of power loss is attributed to straining the material at positive and negative magnetizations[23].

2.3. Commonly Used Soft Magnets for Inductor Cores

The first core materials were laminated iron alloys such as silicon steels and nickel steels. These materials have very high permeability values and are inexpensive; however, their electrical resistivities are relatively low, allowing large eddy currents to form. The main reductions to eddy current losses are through lamination. Laminated cores have smaller eddy current losses but are difficult to produce in complex geometries. Additionally, the presence of silicon or nickel in the steel requires smelting in electric arc furnaces, which drives up energy costs[19,24].

As an alternative, ferrite materials were developed and used as inductor core materials. Ferrite cores are made of iron-based ceramic powders with extremely high electrical resistances that minimize eddy currents. Since most ferrites start in powdered form, the fabrication process for ferrite cores starts with pressing or sintering to achieve a highly dense and homogeneous solid shape[24]. After pressing, the cores are fired in a kiln or oven and further processed to achieve the final shape. Unfortunately, ferrites have around ¼ the saturation magnetization as steels, and therefore struggle to compete in high power applications.

2.3.1. Development of Soft Magnetic Composites (SMCs)

A more recent development in materials for inductor applications includes soft magnetic composites (SMCs). SMCs are clusters of compacted ferromagnetic powders, coated with a thin electrically insulating layer acting as a composite matrix. As discussed earlier, eddy currents can be minimized by laminating the material and by decreasing the electrical conductivity of the material[13]. An SMC achieves exceptionally low eddy current losses because the magnetic powder has a much higher electrical resistivity than other soft magnets, and the insulating layer surrounds each nanoscopic cluster[9]. Additionally, SMC components can be molded into almost any shape, allowing for more design freedom compared to traditional inductors[17].

The biggest drawback to SMC materials is their reduced permeability in comparison to laminated steels[25]. The reasons for this lower permeability are due firstly to the SMCs' nature of having insulated particles that prevent the easy transfer of magnetic flux between them. Secondly, the compaction of the powders at high pressures creates cold working, which negatively affects their permeability[18]. Moving towards higher-density magnetic composites can help mitigate these losses by increasing permeability and saturation magnetization. Despite their reduced permeabilities relative to laminated steels, SMCs outperform laminated steels at high frequencies due to their low eddy current losses as shown in the comparison in Figure 10 [12]. We can expect that the difference in losses between SMCs and laminated steels becomes even more pronounced at even higher frequencies, where SMCs would excel.
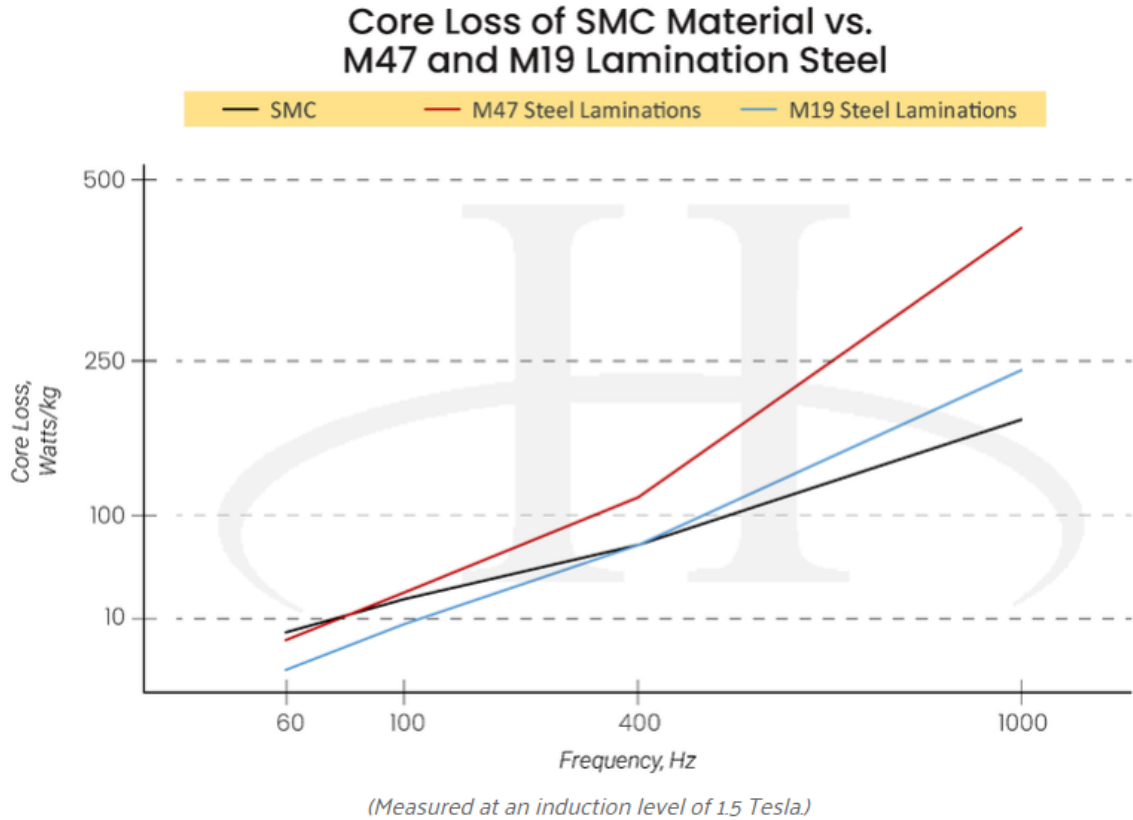
Figure 10. Comparison of overall hysteresis and eddy current losses of a SMC material to laminated steel as a function of frequency. For frequencies above 400 Hz, the SMC experiences less core loss than the laminated steel[12].

2.4. Iron Nitride SMC Inductors

The exploration of viable materials for soft magnetic composites is still early in the research and prototyping phase. Most of the focus on SMC inductors is on iron-based materials that show low core losses. One such material is iron nitride, which shows considerable potential in a variety of applications. Current research at Sandia National Labs focuses on iron nitride in its soft magnetic phase, γ'-Fe_4N, which meets all the requirements for a new soft magnetic material as summarized in Table 1 [2]. γ'-Fe_4N has high magnetic polarization (μM_s), high resistivity (ρ), and low cost[17].

Table 1. Comparison of iron nitride properties to properties of other commonly used soft magnetic materials.

Magnetic Material	μM_s	$\rho(\mu\Omega\cdot m)$	Cost
VITROPERM (Vacuumschmelze)	1.20	1.15	High
Metglas 2605SC	1.60	1.37	High
Ferrite (Ferroxcube)	0.52	5×10^6	Low
Si steel	1.87	0.05	Low
γ'-Fe$_4$N	1.89	> 200	Low

Although iron nitride has yet to be integrated into advanced power circuits, it was recently recognized as an R&D 100 Winner for the 2022 Materials category[26]. Currently the biggest challenge of using pure γ'-Fe$_4$N is developing a straightforward synthesis process due to the metastable nature of iron nitrides[2]. The current synthesis process starts with a gas atomized iron powder that undergoes cryomilling to obtain specific particle sizes. The milled powder is then reacted with ammonia to form iron nitride powder[2]. Once synthesis is achieved, processing is much simpler, involving milling and mixing with epoxy components to form the composite that is then molded into the desired shape.

Iron nitride SMCs are good candidates for the core material because of their low core losses and comparable magnetization to steels[17], as well as their abundant elemental components which minimize environmental impact. Additionally, as power conversion systems become more compact at high frequencies, there is also a need for more electronic and magnetic materials capable of operating at higher temperatures. Iron nitride SMCs not only reduce thermal losses within the device but have excellent performance stability at high temperatures[27].

2.4.1. Existing Work on Iron Nitride SMC Inductors at Sandia

Our sponsor at Sandia National Labs has an existing project that focuses on developing an inductor using phase pure γ'-Fe$_4$N in a composite with a proprietary epoxy. The end goal of the

project is to use the γ'-Fe$_4$N in the inductor to maximize inductance. However, obtaining pure Fe$_4$N powders for use in the prototyping process would be extremely costly due to the complex processing described above. Instead, the team at Sandia decided to use generic Fe$_x$N ($2 < x < 4$) powder to reduce costs and optimize the fabrication of the inductor during the current early prototyping phase of the project. Ultimately the composite made with Fe$_x$N can undergo annealing to obtain the Fe$_4$N phase that is key for stabilization of the face-centered cubic (FCC) γ-Fe structure (Figure 11). The crystal structure in Figure 11 shows the theoretical magnetization as a sum of the Bohr magnetons for each atom (μ_B).
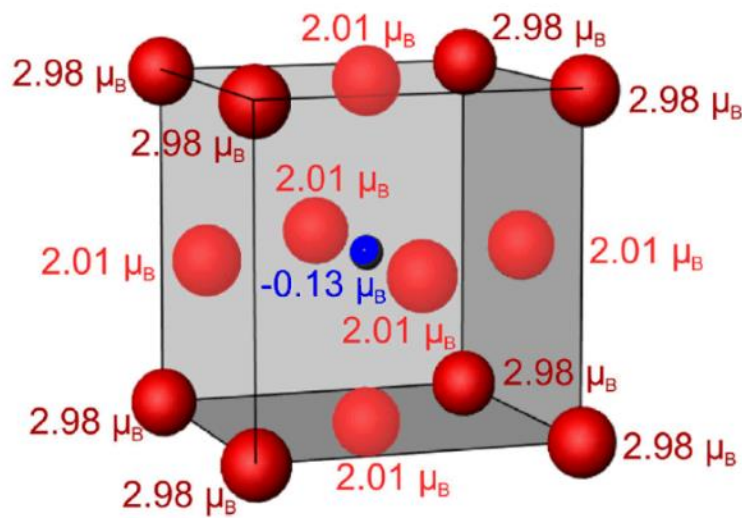
Figure 11. The γ-Fe$_4$N phase has the FCC crystal structure and is stabilized by the interstitial nitrogen in the center of the unit cell[2].

It should be noted that the possible loading conditions of Fe$_4$N in the composite core material are limited by the practical limits of the fabrication process. The initial design of the inductor completed by Sandia was a bobbin inductor, which had the core wound with insulated copper and enclosed in a 0.5 cm thick composite yoke. The bobbin style was originally chosen based on its compact geometry and its ability to reduce temperature coefficient (TC) resistance due to a lower overall length in copper windings. Ultimately, there were many issues with processing the bobbin inductor that outweighed these advantages. Some issues included the inability to achieve high vol% iron nitride in the yoke and the inclusion of voids and bubbles from curing, even at lower iron nitride loading conditions. These defects can be seen on the sides of the bobbin inductor prototype shown in Figure 12. The team working on the inductor at Sandia decided to switch to a toroidal design to decrease processing difficulties and are beginning the initial prototyping of the

new inductor geometry. Fabrication of the toroidal inductors will be much simpler than the bobbin style, and higher vol% iron nitride can be achieved through hot pressing. To speed up the process, this senior project will optimize the design of the toroidal inductor to reduce the number of total iterations in the research process.
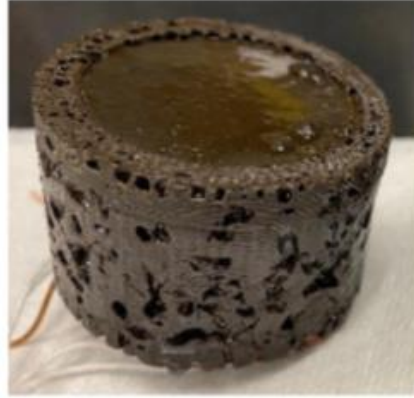
Figure 12. The bobbin inductor design for the inductor prototype included many defects due to the multi-step curing process and the large size (5 cm in diameter, 8 cm in height) of the original inductor design.

To optimize the magnetic performance of iron nitride SMC inductors with respect to geometry and processing, it is necessary to find the relationship between the volume percent Fe_4N and certain magnetic parameters. Assuming our SMC inductor has a toroidal geometry with a rectangular cross section, the inductance (L) should scale linearly with its permeability (μ) through Equation 2.3:

$$L = \frac{\mu N^2 h}{2\pi} \ln\left(\frac{b}{a}\right)$$

Equation 2.3

where *h, a,* and *b* represent the height, inner radius, and outer radius, respectively, of the toroidal inductor (Figure 4). According to Equation 2.3, an ideal inductor will minimize core losses, maximize permeability, and thus maximize inductance. As such, this project will focus on examining how the resistance, permeability, and inductance change as a function of Fe_4N loading in the composite in addition to design considerations such as inductor size, number of wire coil turns (N), and wire thickness.

3. Methods and Materials

Based on the initial problem statement (*what is the optimal size, number of windings, vol% loading of iron nitride, and wire gauge to meet the 600 µH inductance requirement of the inductor?)*, the project was split into two stages. The goal of the first stage was to determine the best combination of toroid size and number of windings to reach 600 µH. This stage used a combination of COMSOL™ and the inductance equation (Equation 2.3) to determine the size and number of windings for the toroid. The next stage focused on a more traditional experiment, where we fabricated several inductors with different combinations of iron nitride vol% loading and wiring thicknesses using the inductor geometry and number of windings determined in the previous stage. This section will go into detail on each stage of the project. The COMSOL™ software used in the project was available through the Cal Poly Remote Desktop in the College of Engineering.

3.1. Modeling in COMSOL™

In general, the toroid model was developed through the series of steps described in Table 2:

Table 2. COMSOL™ modeling usually occurs in the following steps in the given order.

Parameters	Used to change the dimensions and values in the model. Organized in one place rather than changing them as needed within each segment of the model.
Geometry	Used to either build the component using primitive shapes and operations or import geometry information from another CAD software.
Materials	Used to assign material properties for each domain within the component.
Physics	Used to assign the physics for the simulation. For this experiment we used the Magnetic Fields physics found within the AC/DC module of COMSOL™. Specific constraints were set on each domain to obtain the correct boundary conditions.
Mesh	Determines size of mesh. A finer mesh means a more accurate solution but also more computing time.
Study	Used to solve for specific values using given equations. For this experiment, we used a time-dependent frequency domain study to find the inductance and AC resistance at a specific frequency.

3.1.1. Parameters

The starting dimensions of the toroid core were developed using Excel and the inductance equation (Equation 2.3). Working backwards from the inductance target of 600 µH and assuming a starting permeability of 10 (based on data from Sandia), the numerical model in Excel was used

to solve for *h*, *N*, *b*, and *a* using the Solve function. The values were then translated to the parameters list in COMSOL[TM]. The final parameters for the model can be found in Appendix A. The inductors are modeled with fillets that were $\frac{1}{10}(b-a)$ (i.e., one tenth of the core width) to mimic the inductor prototypes which were fabricated with that fillet radius to reduce stress concentrations. The thickness of the coils was determined by the diameter of the wiring and the number of layers, which varied depending on the size of the wiring.

3.1.2. Geometry

The COMSOL[TM] model included a toroidal core surrounded by a continuous, uniform conductor layer to represent the windings. This design is shown in Figure 13 where *h* represents the height of the core, *a* represents the radial distance from the centerline to the inner diameter, and *b* represents the radial distance from the centerline to the outer diameter. The windings are visible as a thin layer over the core with the same thickness as the diameter of the wire used for windings. This layer assumes the windings to be a homogenized multi-turn conductor (HMC) with *N* turns of a tightly wound conductive wire.
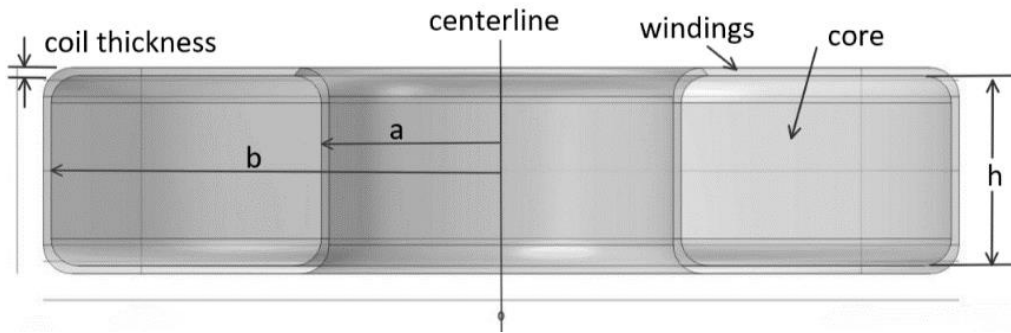
Figure 13. Cross-section of HMC model, showing toroid with key dimensions a, b, and h, and illustration of winding as a continuous, uniform layer around the inductor core.

With the HMC assumption, the geometry was easily simplified and reduced the computing power needed for this model. Additionally, the toroid was enclosed in a sphere of air with a five cm diameter to enclose the inductor in a realistic magnetically insulative environment (Figure 14).
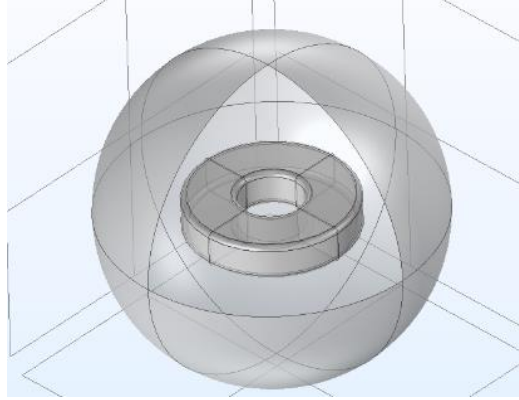
Figure 14. Overall view of the geometry of the HMC toroid inductor model in COMSOL^{TM} with a portion of the air surface hidden so that the inductor is visible.

3.1.3. Materials

The materials of the inductor were assigned based on the domains of the inductor core, windings, and air sphere. The first domain was the core, which was assigned a Blank Material in COMSOL^{TM} to input a relative permeability of 13 for the 65 vol% inductor and 8 for the 50 vol% inductor initially (Figure 15). This value was sourced from data from Sandia for previous iron nitride SMC toroid cores that used iron nitride powder from Alfa Aesar, a different vendor than used in this project. The second domain was the windings, which was assigned the Copper material from the built-in library of materials in COMSOL^{TM}. The third domain used the built-in Air material to enclose the inductor. The full list of material properties used in the model can be found in Appendix A.
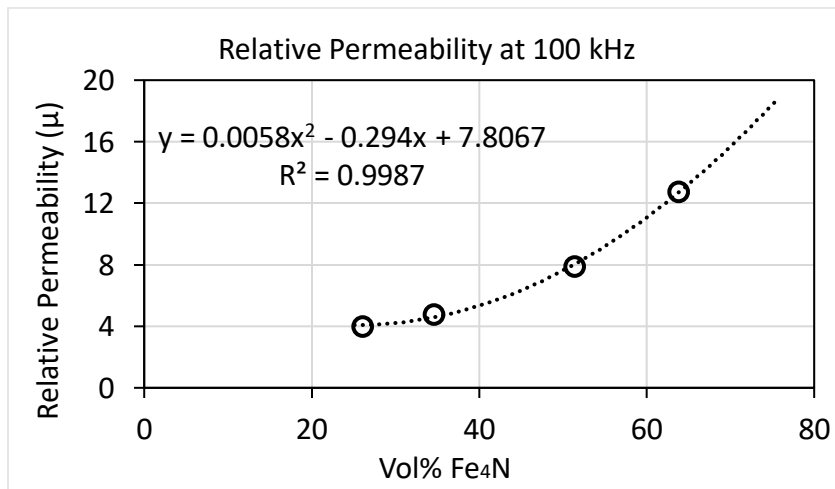
Figure 15. Initial permeability values used in the COMSOL^{TM} model were based on previous permeability data from prototypes made at Sandia.

24

3.1.4. Physics

The physics used for this experiment was the Magnetic Fields (mf) approach that is available as part of the AC/DC module in COMSOL™. We applied several boundary conditions to help COMSOL™ reach the solution, including Magnetic Insulation applied to the boundary of the air sphere, the Coil Geometric Analysis applied to the copper coils to account for the skin effect which can change the conductivity of coiled wires, and Ampere's Law applied to the air sphere and the iron nitride composite core. The full list of boundary conditions and the domains and boundaries they are applied to are listed in Appendix A. The main equations used in the Magnetic Fields approach are:

$$\nabla \times \mathbf{H} = \mathbf{J}$$

Equation 3.1

$$\mathbf{B} = \nabla \times \mathbf{A}$$

Equation 3.2

$$\mathbf{J} = \sigma \mathbf{E} + j\omega \mathbf{D} + \mathbf{J}_e$$

Equation 3.3

$$\mathbf{E} = -j\omega \mathbf{A}$$

Equation 3.4

where $\mathbf{H}$ is the magnetic field, $\mathbf{B}$ is the magnetic flux density, $\mathbf{A}$ is the inductance factor, $\mathbf{J}$ is the magnetic polarization, j is the current density, $\mathbf{E}$ is the electric field, $\mathbf{D}$ is the electric flux density, σ is the surface charge density, and ω is the angular frequency. The Magnetic Fields module generated a series of partial differential equations (PDEs) based on Equations 3.1 - 3.4. These PDEs do not have solutions in closed form for the geometry and conditions of the inductors in this project, so COMSOL™ uses weak formulations of the PDEs to solve them numerically at each node until the results converge.

3.1.5. Meshing

A Fine mesh was used for the finite element analysis (FEA) in COMSOL™ to increase the accuracy of the model while balancing the computing time and power required to solve the model. With a Fine mesh, there are sufficient nodes to solve the PDEs with some accuracy without greatly increasing the computational load. The meshed model is shown in Figure 16.
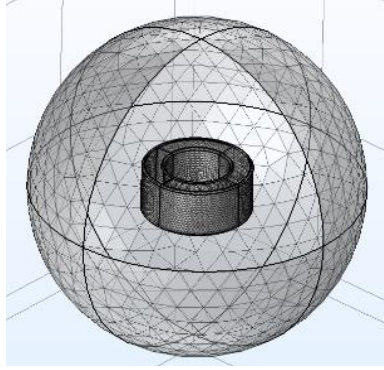
Figure 16. The model uses a Fine mesh as an initial solution to balance computing power and accuracy.

3.1.6. Computational Study

Since many inductor applications use AC at high frequencies, a time-dependent frequency domain study was used to calculate the inductance and AC resistance in COMSOL™. Previous research at Sandia yielded a frequency range of 10-50+ kHz (Figure 17). The 600 µH inductance requirement corresponds to an AC frequency of about 60 kHz so the initial simulation study calculated the inductance and AC resistance at 60 kHz.
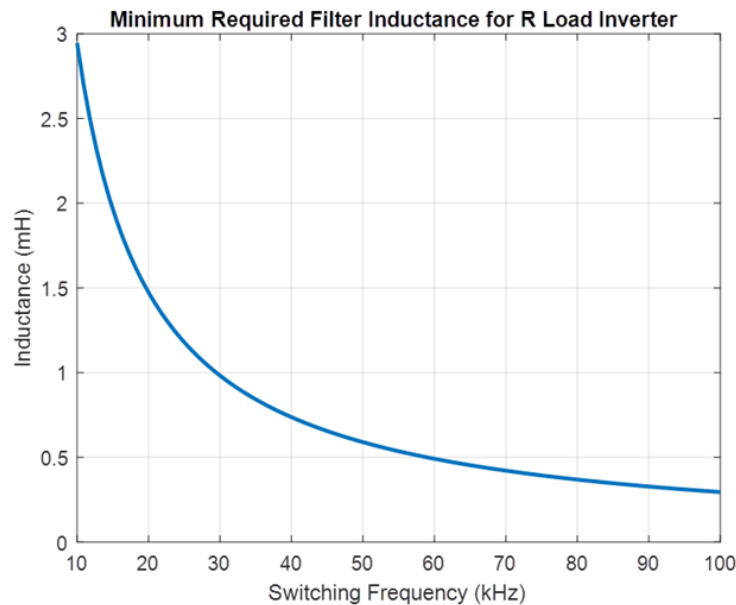
Figure 17. The minimum required filter inductance is dependent on the AC frequency in kHz such that the 600 µH requirement set by our sponsor corresponds to roughly a 60 kHz AC frequency.

Later, during the fabrication process, the inductor prototypes were tested at 1, 10, and 100 kHz due to equipment limitations. To mimic this, later simulations used a new frequency range of 1, 10, 60, and 100 kHz in the time-dependent frequency domain study.

3.2. Experimental Design

Fabrication of toroidal inductors began after determining the initial size and number of windings using the Excel model. Although the model was close to the 600 µH requirement, the amount of material needed to fabricate a toroidal inductor to reach that inductance was beyond the budget of the project. As such, the inductance requirement was decreased to 296 µH and the dimensions of the inductor were adjusted to reduce the amounts of material needed. The general approach to modifying our dimensions focused on minimizing the core volume while maintaining a large inner diameter. A large inner diameter was necessary not only to accommodate a high number of turns of copper winding, but also to allow room for physically hand winding the wire coil. The final dimensions of the fabricated toroid are shown in Figure 18. The number of windings to reach the 296 µH scaled requirement was determined to be 150 turns based on the inner diameter of the toroid.
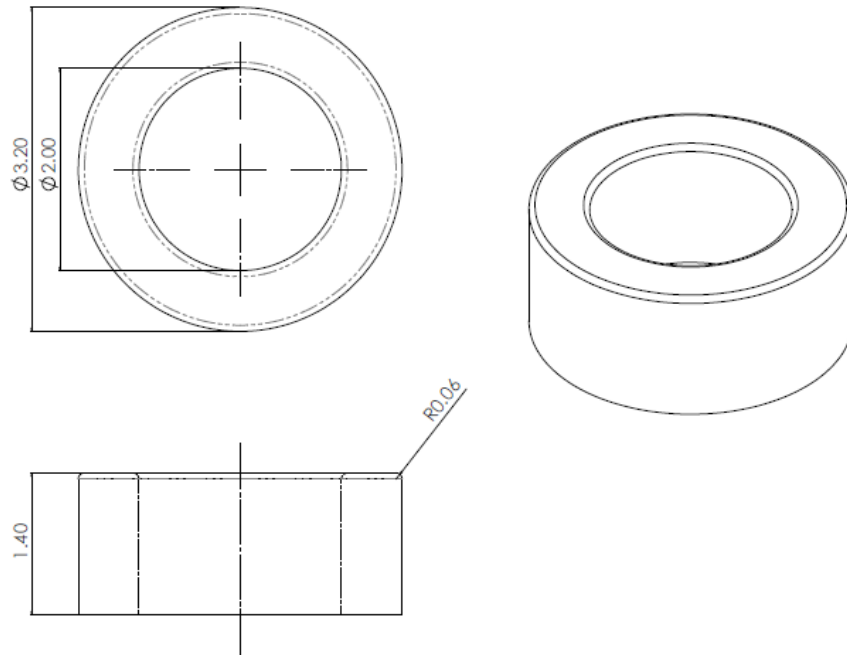
Figure 18. SolidWorks drawings showing the final dimensions of the iron nitride SMC core for fabrication.

Holding the size and number of turns constant for each inductor, an experiment design was developed to determine the best combination of vol% loading of iron nitride and wire sizing to reach the inductance requirement. The design of experiment (DOE) is shown in Table 3 followed by the reasoning for each facet of the design.

27

Table 3. The DOE results in a total of four samples for fabrication.

Factors	Levels	
Vol% of Iron Nitride	65 vol% IN	50 vol% IN
Wiring Size	20 AWG	26 AWG

3.2.1. Sample Size

The greatest limiting factor for the experiment was the amount of available material. Because this project builds upon existing work by Sandia, the materials for the prototypes (iron nitride powder and high-temperature epoxy) were sent directly from Sandia. As such, the sample size was limited to one trial per cell of the DOE (i.e., four total prototypes). This sample size came with several advantages: 1) results from each DOE factor and level were used to validate the model, 2) by changing the parameters of permeability and wire size in the model, the accuracy of the model can be assessed across different combinations of the two experimental factors, and 3) the material amounts and fabrication time were minimized. The main disadvantages of the sample size include the overall lack of statistical significance or high confidence in the results due to the extremely small sample size. There was also limited room to improve processing between each inductor prototype because there were only two inductors of each iron nitride vol% loading.

3.2.2. Vol% Loading of Iron Nitride

65 vol% and 50 vol% loading of iron nitride were studied. 65 vol% loading was chosen because it is the practical loading limit with the current processing method used by Sandia that balances processing requirements with inductance. Above this vol%, the composite is hard to situate into the toroidal mold and is less likely to hold its shape during processing. 50 vol% loading was chosen because it is significantly distinct from 65% (as opposed to 60 vol%) while still having a higher inductance than lower loading percentages such as 30 vol% or 40 vol%.

3.2.3. Wire Size

Two levels of wiring thickness were pursued for winding the cores: 20 AWG and 26 AWG. These sizes were already used for the previous inductor prototypes at Sandia, so the wiring was easily available. 20 AWG wire has a diameter of 0.8128 mm while the 26 AWG has a diameter of 0.4038 mm. Other than size, the difference between the two sizes of wire was the DC resistance,

which can be considered negligible for this experiment as the model mainly used AC resistance data to validate the model.

3.3. Fabrication Procedure

The overall procedure for fabricating the inductor consists of three parts: developing the mold for the toroid core shape, mixing and curing the composite core, and winding the wire around the cured core.

3.3.1. Toroid Mold

The optimized dimensions from Excel were transferred to SolidWorks to build a CAD file of the toroid and its corresponding negative (the antimold) to form the mold. The antimold consisted of two removable wall pieces and a base to make mold release easier (Figure 19). All three pieces of the antimold were 3D printed separately using polylactic acid (PLA) filament.
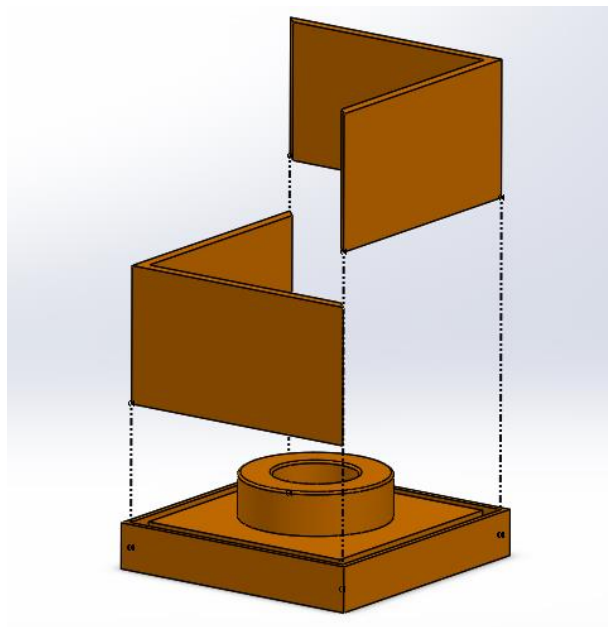
Figure 19. The antimold was designed with 3 separate pieces in SolidWorks and exported into a .stl file to 3D print.

To form the mold, Smooth-Sil 960 silicone rubber was degassed using a degassing chamber and vacuum pump to reduce bubbles. Once mixed and degassed, the liquid silicone was poured into the antimold and left to cure at room temperature for 16 hours. The resulting mold is shown in Figure 20.
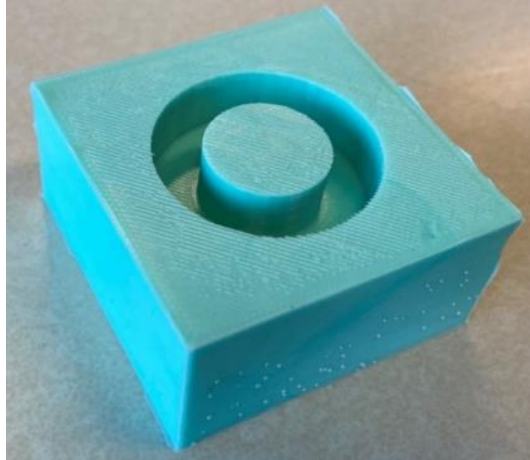
Figure 20. The silicone mold was formed by allowing the degassed liquid silicone mixture to cure in the antimold for 16 hours.

3.3.2. Composite Mixture

The soft magnetic composite used for the inductor is composed of two components: the epoxy matrix and the ferromagnetic particles. The epoxy is made of two compounds that combine to open the epoxide rings and crosslink to form a thermoset epoxy. The first compound is a liquid epoxide, N, N-diglycidyl-4-glycidyloxyaniline (NND), and the second compound is a powder curing agent called 4-aminophenylsulfone (4-AS). The mixing ratio of the two compounds is 0.75 mol NND:1 mol 4-AS. The ferromagnetic particle material is powdered iron nitride from Stanford Advanced Materials with the chemical formula Fe_3N. The iron nitride powder used for this project differs from the powder used in Sandia's previous iron nitride SMC samples as it is from a new vendor (Stanford Advanced Materials) whereas the previous vendor was Alfa Aesar. Currently the iron nitride powder from Stanford Advanced Materials is in the process of being characterized, but key differences are composition and phase: the iron nitride powder used in this project (Stanford Advanced Materials) is Fe_3N while the iron nitride powder used in previous samples was Fe_xN, $2 \leq x \leq 4$. To keep documentation consistent with Sandia, the compound is denoted as "IN" to follow the existing convention set by Sandia. For this project, the vendor for the NND and 4-AS was Sigma-Aldrich. The IN and 4-AS powders were generously sent to Cal Poly from Sandia.

The composite mixture for a single inductor began by mixing the IN and 4-AS powders together to encourage homogeneous distribution of the IN throughout the composite. The powders were milled in a tungsten carbide mill pot on a Spex Sample Prep 8000M Mixer/Miller high energy ball mill for 18 minutes to ensure the powders were mixed sufficiently. The milled 4-AS and IN

were sent to us by our sponsor due to equipment limitations at Cal Poly. The milled powders were added to a 200 mL beaker along with an appropriate amount of NND set by the mixing ratio above to form the epoxy. The beaker was heated to 180°C on a hot plate to melt the 4-AS and combine it with the NND to form the epoxy. After no more than 12 minutes, the composite mixture was transferred to the mold made previously and set in an oven at 120°C for an hour. The composite needed to cure at 180°C for at least 12 hours but to reduce bubbles from the curing process, a ramp process was used to bring the temperature from 120°C to 180°C. Once the composite inductor was completely cured and cooled to room temperature, the core was demolded and sanded. The full procedure can be found in Appendix B.

For each inductor, the total volume of the toroidal shape was 6.86 cm^3 to reach ½ of the inductance requirement with 150 turns in multiple layers. To reduce the volume of the toroid (originally 160.8 cm^3) and thus the amount of material needed, only a percentage of the inductance requirement was used. The breakdown of the materials needed for the inductor samples is shown in Table 4.

Table 4. Amounts of materials used for fabricating the four toroidal inductor samples.

	50 vol %	65 vol%
20 AWG	25.6 g IN, 1.93 g 4-AS, 2.27 mL NND 464 cm wire	33.03 g IN, 1.34 g 4-AS, 1.59 mL NND 516 cm wire
26 AWG	25.6 g IN, 1.93 g 4-AS, 2.27 mL NND 478 cm wire	33.03 g IN, 1.34 g 4-AS, 1.59 mL NND 538 cm wire

3.3.3. Sanding the Inductor

Once the inductor cores were cured and removed from the mold, the dimensions and weight were recorded to calculate the density of the core. Measurements were taken before and after sanding the inductor with 300 grit silicon carbide paper to remove the sharp edges and uneven surfaces that resulted from curing. The inside edges of the core were sanded using a conical surface covered in 300 grit silicon carbide paper to develop a small chamfer as shown in Figure 21. The main purpose of sanding the inductors was to remove any surface inconsistencies and to round the edges to facilitate the winding process.
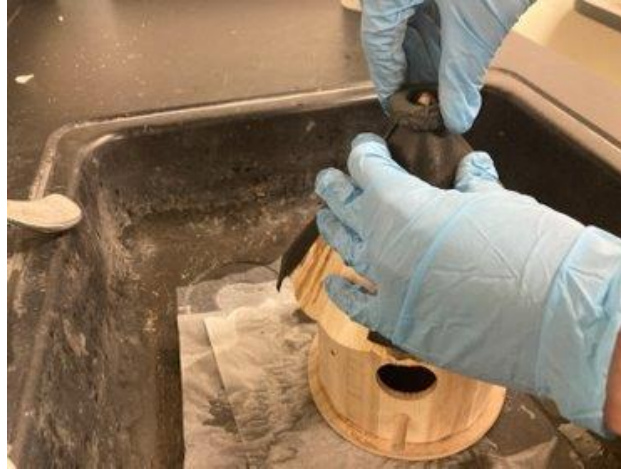
Figure 21. Wet sanding an inside chamfer on cured inductor core using the conical roof of a birdhouse.

3.3.4. Winding the Inductor

The high-temperature copper wiring used for the inductors was sent from Sandia to keep results consistent with future prototypes. Each toroidal inductor was wound by hand for a total of 150 turns for each wire gauge. For the 20 AWG wire, this resulted in three layers of windings because of the larger wire diameter. For the 26 AWG wire, there was a single layer of windings.

3.3.5. Testing and Validation

Testing took place on campus using a DER EE DE-5000 handheld LCR meter in the Student Project Lab in Cal Poly's Electrical Engineering Department. Prior to testing, the insulator coating on the ends of the wires was carefully removed and the exposed wire was covered in solder in a process called "tinning" to improve the connection between the wire and the LCR meter. Due to the limitations of the equipment used, inductance results were taken at 1, 10, and 100 kHz.

4. Results

Like the methodology presented above, the project results are split into two types: experiment and simulation. Initial results from the simulation did not incorporate the exact sizes of the inductor prototype cores nor the effect of defects and voids seen in the fabricated cores, so the model was adjusted to gather new results using the information from the experimental results. Accordingly, the fabrication and experimental results are presented before the simulation results in this section.

4.1. Fabrication Results

Although the inductor fabrication procedure was the same, the 50 vol% and 65 vol% cores differed in several ways throughout the fabrication process, resulting in visual differences that

were quantified by calculating the density of the cores. Additionally, dimensions of all cores varied due to the accuracy of the silicone mold and processing. The full dimensions for all four cores after sanding but before winding are shown in Table 5. Appendix C contains the masses before and after sanding as well as the percent of mass lost for all four inductors.

Table 5. Dimensions of the cores after sanding closely match the target dimensions.

Target	1.12 cm	1.00 cm	1.80 cm
Sample	**Height (cm)**	**Inner Radius, *a* (cm)**	**Outer Radius, *b* (cm)**
65 vol%, 26 AWG	0.94	1.00	1.80
65 vol%, 20 AWG	1.03	0.99	1.79
50 vol%, 26 AWG	0.68	0.99	1.79
50 vol% 20 AWG	0.73	1.00	1.80

4.1.1. 50 vol% inductor fabrication

During the mixing phase, the mixture of 4-AS, NND, and 50 vol% IN quickly melted into a viscous liquid on the hot plate. The liquid was then poured into the silicone mold to cure. However, due to the adhesion of the liquid to the 200 mL glass beaker's surface, a significant amount of 50 vol% mixture was lost to the inside of the beaker, where the composite mixture tended to adhere to the walls (Figure 22). Specifically, a mass loss of 30% and 25% of material was observed for the first and second 50 vol% cores, respectively, during this transfer step. This resulted in the mixture only partially filling the mold, which produced a toroid with a smaller height than intended, with no extra mixture easily extractable from the beaker to ensure proper toroid height. Once in the silicone mold, the liquid mixture leveled out automatically due to gravity without the need for manual packing. Once cured, the 50 vol% inductor had a relatively smooth surface upon demolding, requiring relatively little sanding except to chamfer the edges. The cores of the 50 vol% inductors had a small, shiny surface on the top face of the core where the material was not covered by the mold (Figure 23). The shiny surface of the 50 vol% was seen before sanding and in the inside surface of the void in the right picture of Figure 23. This may be due to the lower vol% of iron nitride in the epoxy, where the lower viscosity of the mixture allowed the iron nitride powder to sink to the bottom of the mold. This separation by density is consistent with subsequent DC resistance measurements of the cores.
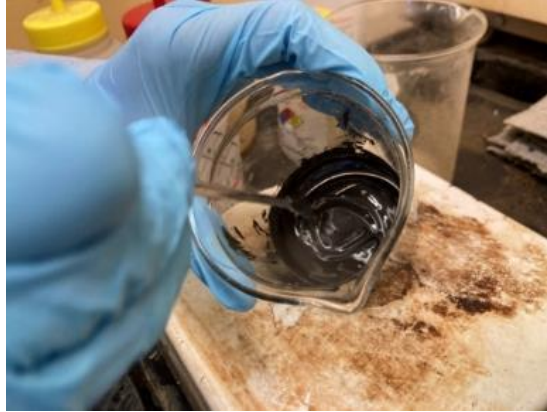
Figure 22. The 50 vol% mixture was a viscous liquid that was easily mixed on the hot plate.
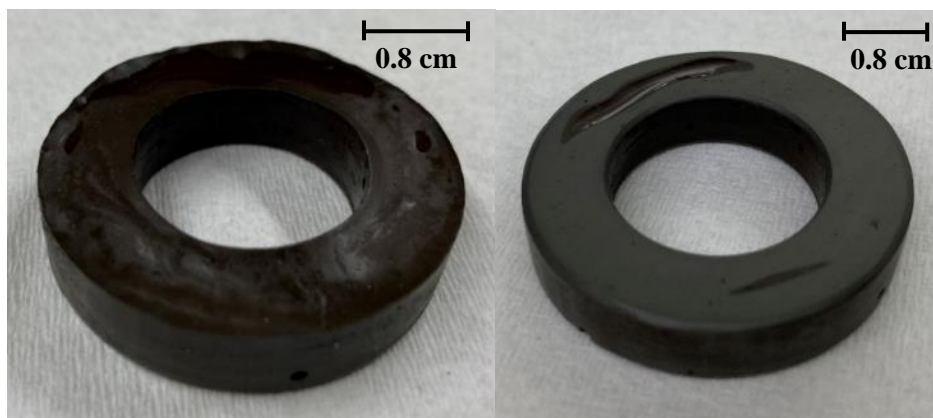
Figure 23. (Left) Top view of the first 50 vol% inductor (to be wound with 20 AWG) before sanding down the uneven surfaces. (Right) Top view of the same inductor showing the shiny inside surface of the long void near the top of the inductor after sanding.

4.1.2. 65 vol% inductor fabrication

In contrast, during the mixing phase for the 65 vol% IN inductors, the mixture remained as powdery clumps that were difficult to mix (Figure 24). Transfer to the mold required packing down the mixture into the mold using a metal spatula to reduce voids and to develop a level surface. Due to its viscosity, the density of the cured composite was influenced significantly by how well the clumps could be packed into the edges of the mold (Figure 25). As such, the porosity of the cured cores was highly variable. In contrast to the 50 vol% mixture, nearly all the 65 vol% mixture was transferred from the 200 mL glass beaker to fill the mold as it was much easier to scrape out of the beaker. Once cured, the 65 vol% core had a flaky surface and many visible voids on its outside surface. These cores lost more mass as more sanding was required to remove or level out surface defects on all its faces. Figure 26 shows the first 65 vol% core before and after sanding.

Unlike the 50 vol% cores, the voids in the 65 vol% core did not appear shiny. In addition, the outside surface of the core appeared dark blue in color, in contrast to the very dark gray/black color of the 50 vol% material. The dark blue color of the 65 vol% material may be due to the higher vol% loading of IN interacting with the atmosphere. This blue coloration appeared only after the curing process and was completely removed through sanding the surface. Further investigation should be done to determine the cause of the dark blue color to see if it is only present in the new vendor of iron nitride powder and at high volume percents.

Figure 24. The 65 vol% mixture was harder to melt because of its clay-like nature associated with the higher vol% loading.
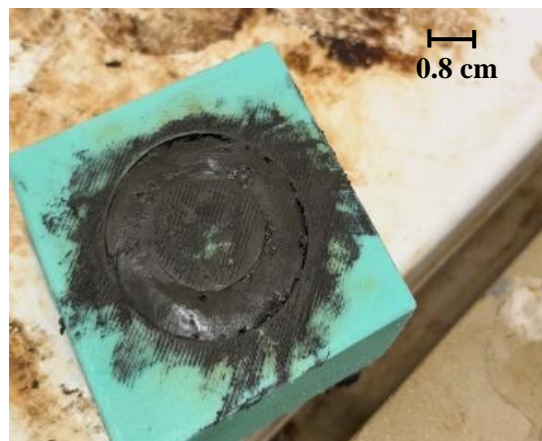
Figure 25. The quality of the 65 vol% cores depended on how well the mixture was packed into the mold, which increased processing time.
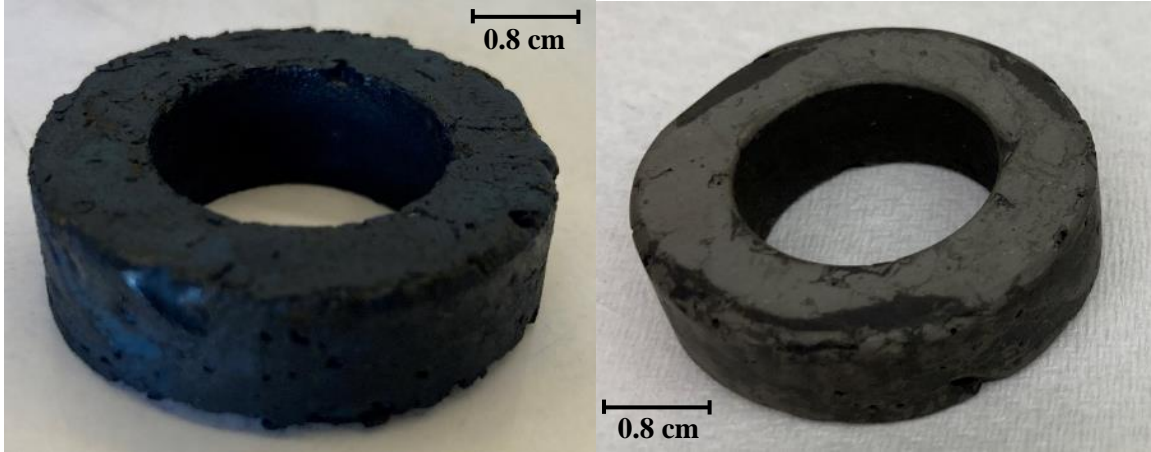
Figure 26. (Left) Close-up of the first 65 vol% core produced (to be wound with 20 AWG wire) showing the rough surface and numerous voids present at the outer surface. (Right) The same inductor after sanding, with some reduced surface roughness but still showing many voids.

4.1.3. Porosity and Effective Vol%

To quantify the amount of voids present in each prototype inductor, the porosity was calculated by comparing the actual density of each core to its theoretical density without voids. This porosity value was then translated into a lower effective vol% of IN by multiplying the vol% by the porosity, since porosity results in less active magnetic material to contribute to its inductance. As seen in Table 6, the 65 vol% prototypes had higher porosity values due to presence of more voids from processing. In addition, the 26 AWG inductors were fabricated before the 20 AWG inductors. The experience and learnings derived from making the 26 AWG inductors were applied to making the 20 AWG inductors, resulting in a significant reduction in voids in the 20 AWG inductors due to faster processing (e.g., less time between first mixing and transferring to mold) and better packing of the mixture into the mold.

Table 6. Calculated effective vol% loading in each inductor prototype.

Fabrication Order	Inductor Prototype	Porosity	Effective Vol%
1st	65 vol% IN 26 AWG	12%	58
2nd	50 vol% IN 26 AWG	5%	48
3rd	65 vol% IN 20 AWG	6%	61
4th	50 vol% IN 20 AWG	3%	49

4.2.   Testing Results

The final inductors after winding and tinning are shown in Figure 27. The inductance and AC resistance values for each prototype were measured using the LCR meter at 1, 10, and 100 kHz (Table 7). Inductance results at 60 kHz were interpolated from the data to match the 60 kHz requirement set by Sandia. The AC resistance results were not interpolated to 60 kHz because of the sharp increase at 100 kHz and should be measured directly in the future where possible. The 20 AWG and 65 vol% prototype has the highest inductance results due to the high vol% loading and lower AC resistance losses. The small drop in inductance from 1 to 100 kHz indicates that inductance is relatively independent of frequency in this range (Figure 28). This independence suggests low eddy current losses in all prototypes, likely due to the high electrical resistance of the SMC core. The AC resistance tended to increase significantly at 100 kHz, indicating the presence of the skin effect where the current density in the wiring is greatest near the outside surface of the wire. One anomaly is the AC resistance result for the 50 vol% core wound with 26 AWG, where the AC resistance is less than one and differs from the results at 100 kHz. One possible reason is lower eddy current losses due to the lower vol% loading in that inductor (effectively 48%). The other 50 vol% inductor also gave a lower AC resistance result, which may also stem from lower eddy current losses compared to the 65 vol% inductors. Additionally, the AC resistance results are consistent with the resistances calculated from the length and thickness of copper wire. This confirmed that the insulative coating remained intact and no short circuits were generated during the winding process.
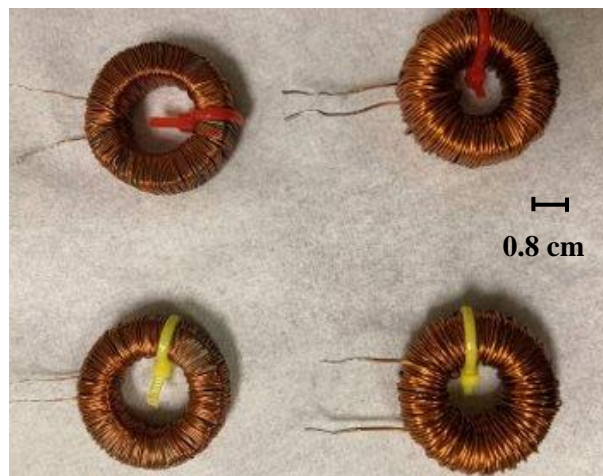
Figure 27. Comparison of finished inductors. On the left are the 26 AWG, 65 vol% (red/top) and 50 vol% (yellow/bottom) inductors. On the right are the 20 AWG, 65 vol% (red/top) and 50 vol% (yellow/bottom) inductors.

Table 7. Measured inductance and AC resistance results for fabricated inductors. The results for 60 kHz (*) are interpolated from the other results.

Inductor Prototype	Frequency (kHz)	Inductance (µH)	AC Resistance (Ω)
65 vol% IN (58 eff. vol%) 26 AWG	1	185.3	0.759
	10	184.73	0.844
	60*	184*	
	100	183.21	7.344
65 vol% IN (61 eff. vol%) 20 AWG	1	226.1	0.275
	10	224.9	0.568
	60*	220*	
	100	216.9	22.2
50 vol% IN (48 eff. vol%) 26 AWG	1	99	0.672
	10	98.17	0.691
	60*	98*	
	100	97.82	0.966
50 vol% IN (49 eff. vol%) 20 AWG	1	120.3	0.241
	10	119.36	0.307
	60*	118*	
	100	116.39	1.95
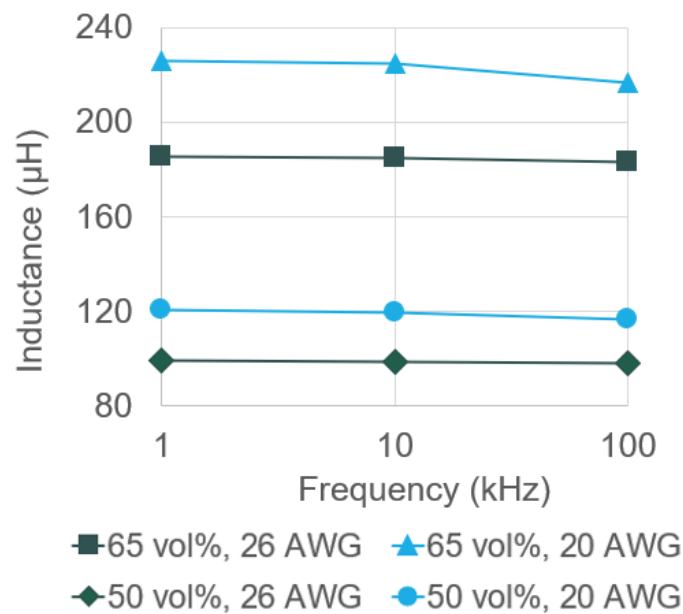
Figure 28. The inductance results show a weak frequency dependence, which may indicate low eddy current loss in the core.

4.3. Simulation Results

The initial simulation included the expected dimensions of the fabricated cores ($h = 1.12$ cm, $a = 1$ cm, and $b = 1.8$ cm) with 150 turns of the copper wiring and an assumed permeability of 10 for the 65 vol% cores and 7 for the 50 vol% cores. After measuring the fabricated inductors, the COMSOL™ simulation was adjusted to reflect the actual dimensions of the inductors shown in Table 5.

The biggest challenge in the model was accounting for core losses through either eddy currents or hysteresis. Electrical conductivity of the core in S/m was used to address eddy current losses and permeability of the core was used to address the hysteresis loss that correlates with coercivity. There were three electrical conductivities and three permeabilities used for each modeled inductor, resulting in a total of 36 iterations in COMSOL. (Table 8). Each iteration had a single parameter changed at a time to identify the effect of permeability and electrical conductivity on inductance and AC resistance results from the model. The results from the 36 iterations are categorized by permeability value used into three models described below. Appendix D contains the results from all 36 iterations.

Table 8. Six different values across two parameters of the IN SMC core were varied to determine the effects on the inductance and AC resistance results.

Parameter	65 vol%, 26 AWG	65 vol%, 20 AWG	50 vol%, 26 AWG	50 vol%, 20 AWG
Permeability	10	10	7	7
	10.12	11.66	6.95	7.28
	8.1	8.1	6.1	6.1
Electrical Conductivity (S/m)	1E-6	1E-6	1E-6	1E-6
	3000	3000	3000	3000
	0.2	0.2	0.01	0.01

4.3.1. Permeabilities Used in COMSOL™ Model

The values for the permeabilities came from three sources. The first permeabilities considered for the model were estimated values from previous IN SMC prototypes made at Sandia, resulting in permeabilities of 10 and 7 for the 65 vol% and 50 vol% cores respectively. The second permeabilities considered were interpolated from previous prototypes using the data shown in

Figure 15. Table 9 shows permeability values used in COMSOL™ that were interpolated based on the porosity and effective vol% values presented in Table 6.

Table 9. The second set of permeability values for the COMSOL™ model were interpolated based on the effective vol% and previous permeability values for other prototypes (Figure 15).

Expected Vol% IN and Windings	Effective Vol% IN	Interpolated Permeability (μ_r)
65 (26 AWG)	58	10.12
65 (20 AWG)	61	11.66
50 (26 AWG)	48	6.95
50 (20 AWG)	49	7.28

The third set of permeability values considered in the model were calculated from the experimental inductance results shown in Table 7. The form of Equation 2.3 used to calculate the permeabilities is shown at the top of Table 10 along with the results. The permeabilities used in the model correspond with the 60 kHz result for the 20 AWG prototypes above (8.1 for 65 vol% and 6.1 for 50 vol%, highlighted in Table 10). The results from the cores wound with 20 AWG wire were used as an upper limit on permeability, as the 26 AWG samples had increased AC resistance due to their smaller wire diameter.

Table 10. The third set of permeabilities were calculated from the experimental results.

$$L = \frac{\mu N^2 h}{2\pi} ln\left(\frac{b}{a}\right) \rightarrow \mu = \frac{2\pi L}{N^2 h \ln(\frac{b}{a})}$$				
	Permeability (26 AWG)		**Permeability (20 AWG)**	
Frequency (kHz)	**65 vol%**	**50 vol%**	**65 vol%**	**50 vol%**
1	7.5	5.5	8.3	6.3
10	7.5	5.5	8.3	6.2
60	7.4	5.5	8.1	6.1
100	7.4	5.5	8.0	6.1

4.3.2. Electrical Conductivities Used in COMSOL™ Model

Like the permeability values, the electrical conductivity values used in the model were sourced from a combination of theory and experiment. The first electrical conductivity value considered was 1 μS/m and was based on similar existing research in modeling an iron nanocomposite

microinductor in COMSOL[29]. The resistivity of the iron nanocomposite was measured using a four-point probe and found to be highly resistive because of the epoxy matrix. With the similar composite makeup of the inductor in this project, the value of 1 μS/m was used as a lower bound on the electrical conductivity to represent the expected highly resistive nature of the composite.

For the upper bound of electrical conductivity, a value of 3000 S/m was derived from Table 1 where the resistivity for pure Fe_4N is 200 μΩ-m or 5000 S/m. The value was lowered from 5000 S/m to 3000 S/m to account for the increased resistivity of the epoxy matrix that makes up 35 - 50% of the composite composition by volume. This value was also adjusted to account for potential differences in the iron nitride composition that may have resulted from the use of the new vendor for the iron nitride powder. The value of 3000 S/m was not meant to accurately capture the resistivity of the core but instead served as an upper bound over nine orders of magnitude of electrical conductivity values.

Since the conductivity values assumed for the core material varied by many orders of magnitude, it was difficult to narrow down the value looking at only inductance and AC resistance results. In addition, a lack of data on iron nitride SMC's electrical conductivity prompted interest in taking measurements directly from the fabricated prototypes. Using the 26 AWG toroids (where some of the core surface is exposed), a total of 10 DC resistance measurements were taken with an ohmmeter: 5 measurements on the toroid's top surface, and 5 measurements on its bottom surface. These measurements were taken at the midpoint between the inner diameter and outer diameter, 180 degrees apart, (12:00 and 6:00 positions on the toroid) and averaged together. It was necessary for the ohmmeter probes to be pressed firmly into the iron nitride SMC's surface for the ohmmeter to read an unchanging value. It was observed that when the multimeter probes gently touched the surface of the core, the DC resistance values were significantly higher than when the probes were pressed firmly into the surface. Measurements on the 20 AWG samples were not possible because the surface was entirely covered by the windings.

Treating the resistance values as a measurement of two linear resistors in parallel, the estimated DC conductivity of the core material was calculated using Equation 4.1:

$$\sigma = \frac{l}{RA}$$

Equation 4.1

In Equation 4.1, l is the expected path length around half the toroidal core, R is the DC resistance measurement, and A is the cross-sectional area of the core. The conductivities of the 50 vol% and 65 vol% cores were calculated to be 0.01 S/m and 0.2 S/m, respectively.

Table 11. DC Resistance measurements of 26 AWG toroidal prototypes

	DC Resistance (kΩ)	
	50 vol%	**65 vol%**
Top Surface	136.0	5.2
	162.0	6.6
	96.0	2.5
	95.0	4.2
	158.0	3.2
Bottom Surface	64.0	1.8
	54.0	2.9
	119.0	2.2
	93.0	4.4
	41.0	3.0
Average	**101.8**	**3.6**

Aside from the small sample size used in the DC resistance measurements, it should be noted that this method of measuring the electrical conductivity of a toroid captures only the DC component of conductivity. The AC component of conductivity is ideally measured with the inductor under operating conditions (e.g., with its operating current flowing). Due to equipment limitations, it was not possible to make this measurement at Cal Poly. However, the relative results were consistent, where the electrical conductivity was around 20 times higher in the 65 vol% sample compared to the 50 vol% sample due to the lower amount of resistive epoxy present. In addition, the top surface of the inductor (not in contact with the mold) had a higher resistivity on average, especially in the 50 vol% inductor. This indicates probable non-uniformity of composition and conductivity throughout, as a higher proportion of epoxy may be present at the top surface of the toroid from curing. The 50 vol% inductors saw a higher difference between the DC resistance measurements taken on the top and bottom surfaces of the inductor likely because the relatively low viscosity of the composite mixture allowed for the denser iron nitride to settle at the bottom rather than remain homogeneously distributed throughout the core. These results

correlate with the observations made about the shininess of the voids and top surface of the 50 vol% cores before winding, indicating separation of materials by density.

These four values of electrical conductivity were used in the simulations in the absence of measured values of electrical conductivities for each of the core materials. There are concerns, however, about how accurately these three values of electrical conductivity represent the core materials: $\sigma = 1$ µS/m and $\sigma = 3000$ S/m were estimated from theoretical values and $\sigma = 0.2$ S/m for the 65 vol% cores and 0.01 S/m for the 50 vol% cores were measured with a small sample size and limited only to DC resistance. Simulations using $\sigma = 1$ µS/m and $\sigma = 3000$ S/m are regarded as estimating the inductance and AC resistivity of the inductors under "bookend" electrical conductivity values.

4.3.3. Model One: Estimated Permeability from Previous Prototypes

The first model used as a starting point the estimated permeabilities μ_r from previous iron nitride SMC prototypes where μ_r for the 65 vol% was assumed to be 10 and μ_r for the 50 vol% was assumed to be 7, resulting in the inductance results shown in Table 12. Initially, the electrical conductivity of the core was given a value of 1 µS/m to represent the extremely high resistance that was initially assumed for a material consisting of iron nitride particles suspended in the epoxy matrix of the SMC. This assumption made the inductance results frequency independent, shown by the same values at each frequency in Table 12. The table also shows the AC resistance results at the frequencies of 1, 10, and 100 kHz and the percent differences between the experimental results described in the previous section to indicate the degree of validity of the assumed permeabilities and electrical conductivity.

The percent differences between model and experiment for inductance range from about 20% - 30% while the percent differences between model and experiment for AC resistance are as high as 196%, indicating that this model was not accurately capturing the losses in the inductor core, especially at high frequencies. The experimental results show a sharp increase in AC resistance at 100 kHz that is not reflected in this model, likely due to the electrical conductivity value assumed for the core. However, one anomaly stands out for the 50 vol%, 26 AWG inductor at 100 kHz, where the percent difference is much lower than the other percent differences at 100 kHz. This low percent difference corresponds to the experimental result of an AC resistance of less than 1 Ω for that inductor at 100 kHz. As explained in the experimental results section, this may be a result

of the lower vol% loading in that inductor, resulting in lower eddy current losses and therefore lower AC resistance readings. This behavior is not shown in the model using this electrical conductivity. To investigate the other values for conductivity, σ was adjusted across the four values described previously (1 μS/m, 0.2 or 0.01 S/m, and 3000 S/m). The results from these iterations are shown in Figures 29 and 30.

Table 12. Results from the first model showing the % differences between model and experiment in inductance and AC resistance. An initial electrical conductivity of 1 μS/m was assumed.

Model	Frequency (kHz)	Inductance (μH)	% Difference in Inductance	AC Resistance (Ω)	% Difference in AC Resistance
65 vol%	1	246.65	28%	0.67049	12%
26 AWG	10	246.65	29%	0.67058	23%
($\mu_r = 10$)	100	246.65	30%	0.67157	166%
65 vol%	1	280.95	22%	0.2123	26%
20 AWG	10	280.95	22%	0.2132	91%
($\mu_r = 10$)	100	280.95	26%	0.2214	196%
50 vol%	1	125.07	23%	0.56651	17%
26 AWG	10	125.07	24%	0.56657	20%
($\mu_r = 7$)	100	125.07	24%	0.56721	52%
50 vol%	1	142.01	17%	0.18317	27%
20 AWG	10	142.01	17%	0.1835	50%
($\mu_r = 7$)	100	142.01	20%	0.18685	165%

Figures 29 and 30 show that a higher electrical conductivity of 3000 S/m causes the inductance and AC resistance to become frequency dependent, albeit weakly for the inductance results. Similar analyses were conducted for later models to see if the trends continued across all permeabilities. Additionally, in this model the confidence level of the permeabilities was low because the permeabilities were estimated based on data gathered from different iron nitride SMC samples made at Sandia that used a different iron nitride powder from a different vendor. Thus, the subsequent model iterations focused on using different values for permeability.

4.3.4. Model Two: Interpolated Permeabilities from Previous Prototypes

The second model used the interpolated permeabilities from previous prototypes shown in Table 9. Like the first model, electrical conductivities of 1 µS/m, 0.2 and 0.01 S/m, and 3000 S/m were used for the core materials, with subsequent analyses on the effect of electrical conductivity on the inductance and AC resistance results. The results of the simulation for the second model are presented in Table 13 along with the percent difference results from the experiment.
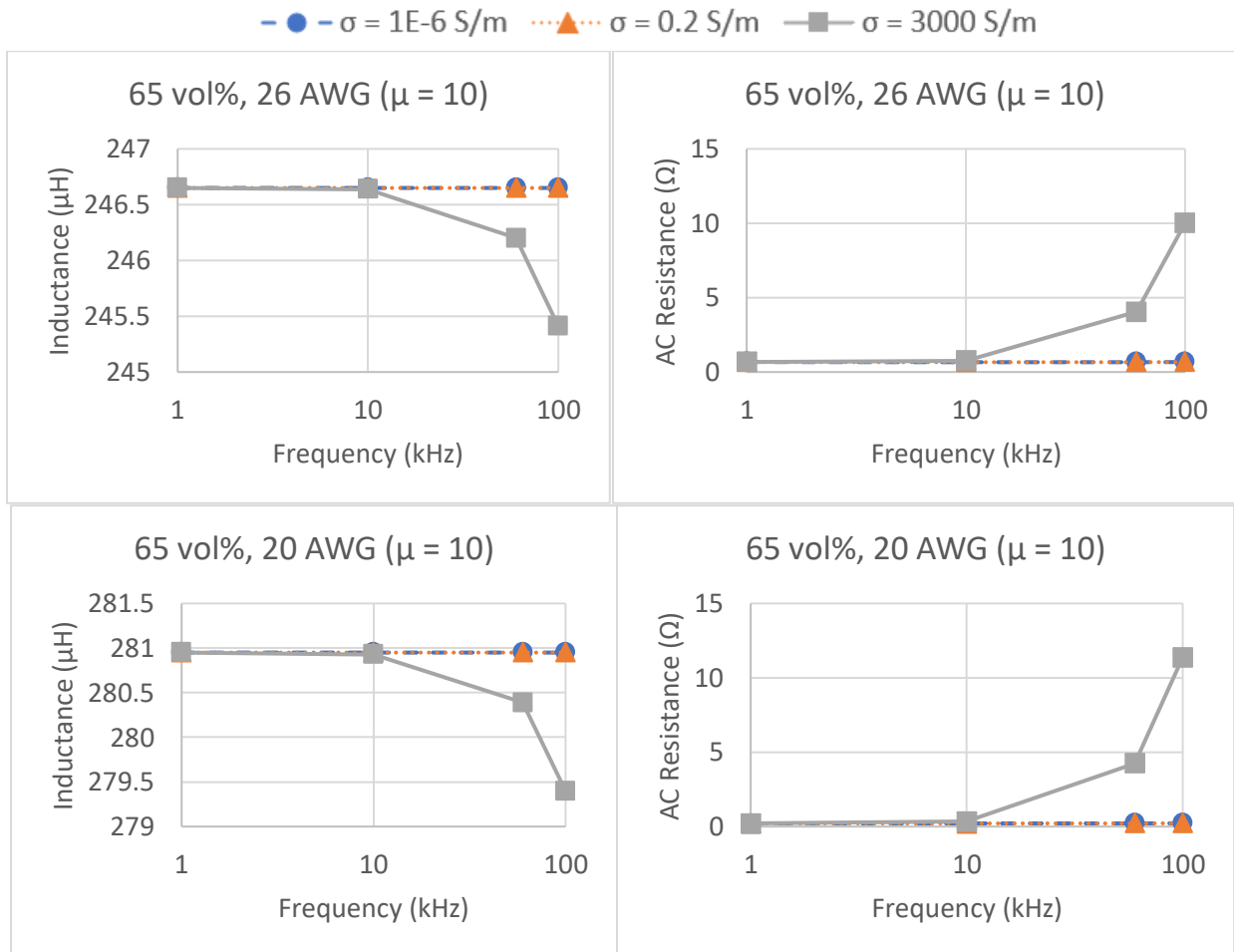
Figure 29. Effect of electrical conductivity on inductance and AC resistance results for 65 vol% model using μ = 10.
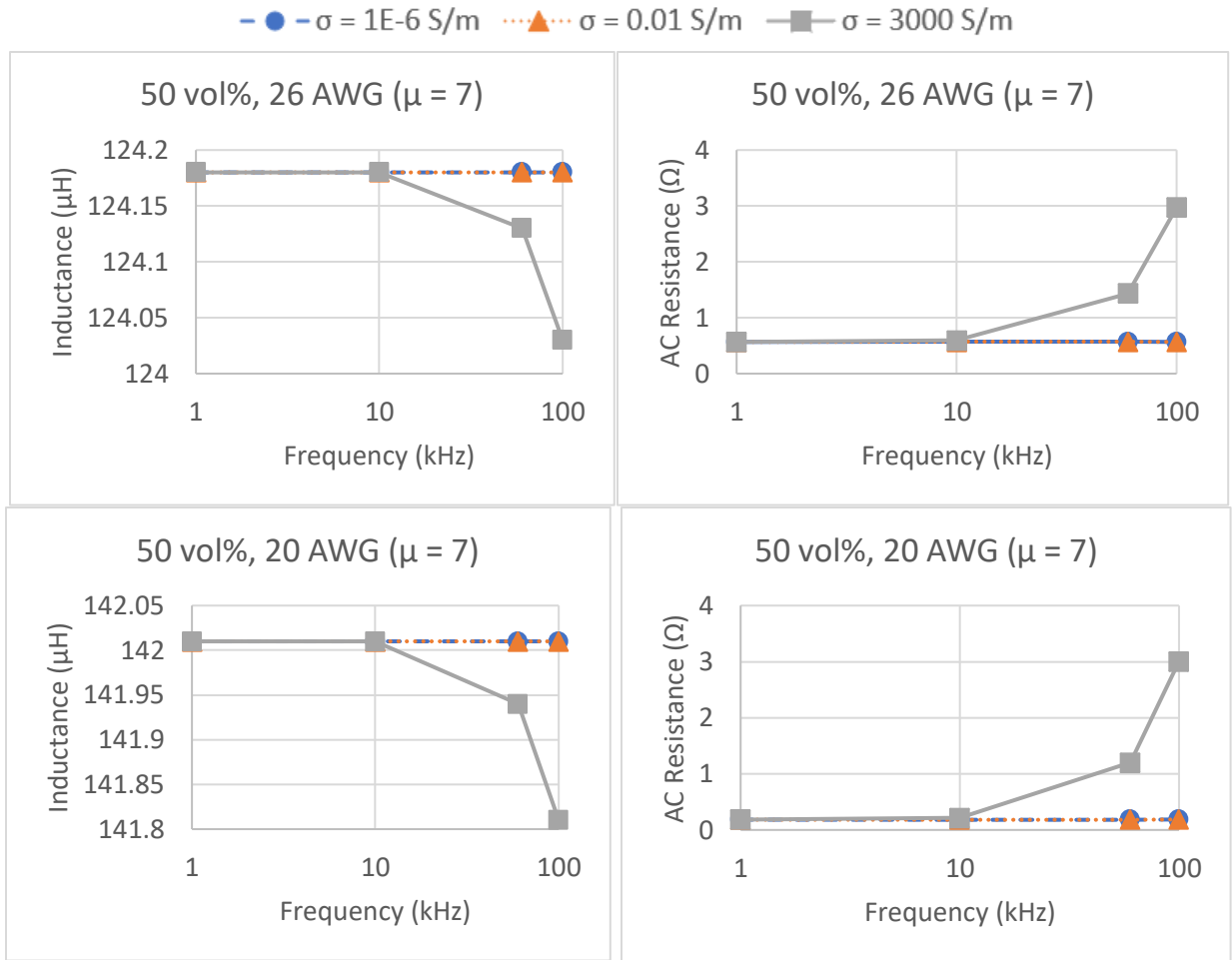
Figure 30. Effect of electrical conductivity on inductance and AC resistance results for 50 vol% model using μ = 7.

The percent differences in inductance between model and experiment in the second model ranged from 24 - 50%, indicating that the model was again not capturing core losses accurately. Similar to the first model, the percent differences for the AC resistances in this model ranged widely and are typically large, indicating that this model does not accurately predict the measured AC resistance values. Interestingly, the AC resistance results were the same as the first model that used σ = 1 μS/m. To verify that this trend continued with the other electrical conductivity values, the same iterative analysis process was completed for μ = 10 and 7 (Figures 31 and 32).

Using an electrical conductivity value of 1 μS/m, the AC resistance values for the interpolated permeabilities are the same as those for the estimated permeabilities. This trend suggests both the inductance and AC resistance are independent of frequency at low electrical conductivities, and gain a weak frequency dependence at high electrical conductivity.

Table 13. Results from the second model that used interpolated permeabilities. An electrical conductivity of 1 μS/m was assumed.

Model	Frequency (kHz)	Inductance (μH)	% Difference in Inductance	AC Resistance (Ω)	% Difference in AC Resistance
65 vol%	1	249.6	35%	0.67049	12%
26 AWG	10	249.6	35%	0.67058	23%
($\mu_r = 10.12$)	100	249.6	36%	0.67157	166%
65 vol%	1	325.69	44%	0.2123	26%
20 AWG	10	325.69	45%	0.2132	91%
($\mu_r = 11.66$)	100	325.69	50%	0.2214	196%
50 vol%	1	124.18	25%	0.56651	17%
26 AWG	10	124.18	26%	0.56666	20%
($\mu_r = 6.95$)	100	124.18	27%	0.5672	52%
50 vol%	1	147.31	22%	0.1832	27%
20 AWG	10	147.31	23%	0.1835	50%
($\mu_r = 7.28$)	100	147.31	27%	0.1871	165%
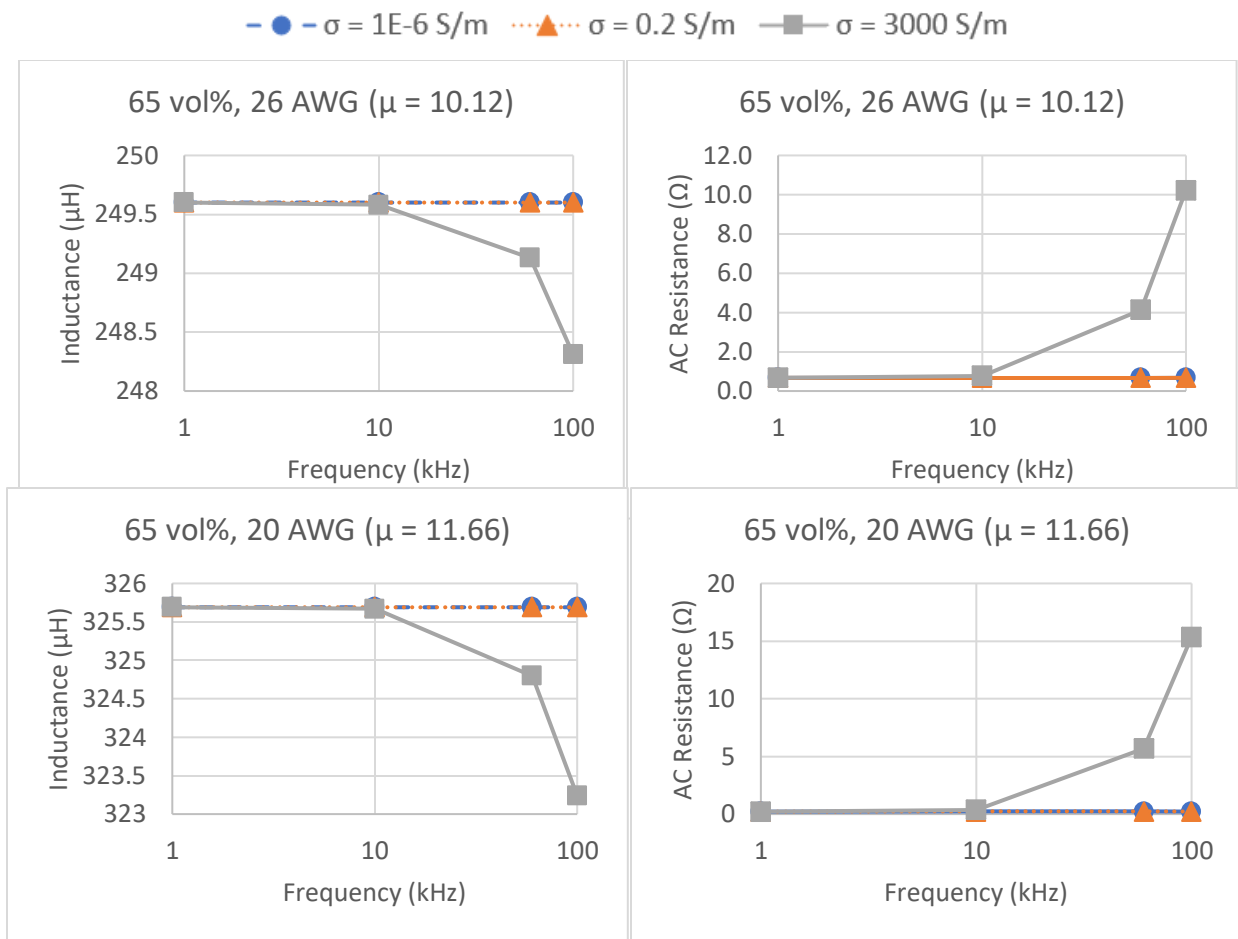
Figure 31. Effect of electrical conductivity on inductance and AC resistance results for 65 vol% model using μ = 10.12 and 11.66.
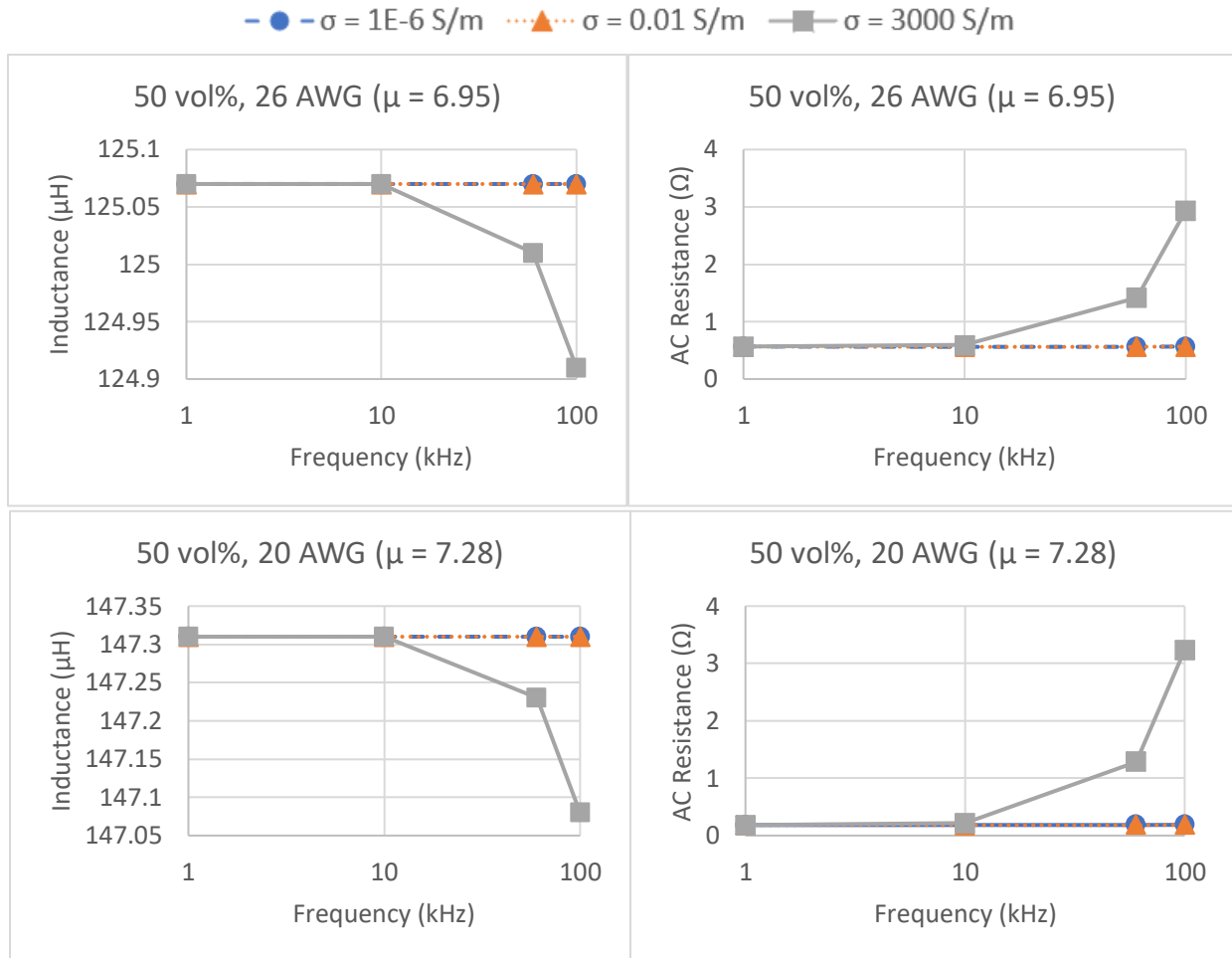
Figure 32. Effect of electrical conductivity on inductance and AC resistance results for 50 vol% model using μ = 6.95 and 7.28.

These permeability values were interpolated rather than estimated, and the interpolation process used a data set of four samples in Figure 15. It is possible that there is a wide variance in permeability for each of the samples referred to in Figure 15, which decreases the confidence level for these permeabilities slightly. Additionally, the data shown in Figure 15 are from previous samples at Sandia, which may have differing IN compositions and therefore differing permeabilities. The samples in this project are the first prototypes to use a new vendor for iron nitride, meaning the use of data from previous samples for permeability values may be a poor assumption.

4.3.5. Model Three: Calculated Permeabilities from Experimental Results

The third iteration of the simulation used permeabilities that were calculated from the experimental inductance values using Equation 2.3 and shown in Table 10. These permeabilities

resulted in the smallest percent differences between the experimental and simulation results (Table 15). The permeability used in this model corresponded to the highlighted values in Table 10 (8.1 for 65 vol% material and 6.1 for 50 vol% material). Simulations with the third model used electrical conductivities of 1 μS/m, 0.2 and 0.01 S/m, and 3000 S/m for the core materials, and subsequent analyses were performed for each value of electrical conductivity to verify that the trends seen in inductance and AC resistance continue.

Table 14. The calculated permeabilities resulted in the smallest percent differences between experimental and model results. An electrical conductivity of 1 μS/m was used once again for this model.

Model	Frequency (kHz)	Inductance (μH)	% Difference in Inductance	AC Resistance (Ω)	% Difference in AC Resistance
65 vol%	1	199.96	8%	0.67049	12%
26 AWG	10	199.96	8%	0.67058	23%
($\mu_r = 8.1$)	100	199.96	9%	0.67157	166%
65 vol%	1	229.73	2%	0.2123	26%
20 AWG	10	229.73	2%	0.21315	91%
($\mu_r = 8.1$)	100	229.73	6%	0.22137	196%
50 vol%	1	107.56	8%	0.56272	18%
26 AWG	10	107.56	9%	0.56277	20%
($\mu_r = 6.1$)	100	107.56	9%	0.56325	53%
50 vol%	1	124.99	4%	0.18316	27%
20 AWG	10	124.99	5%	0.18342	50%
($\mu_r = 6.1$)	100	124.99	7%	0.18601	165%

The third model resulted in some of the lowest percent differences between the simulation and the prototypes, with a range of 4 - 9% for the inductance results and again, 12 - 196% for the AC resistance results. As with the first two models, further analyses on the effect of electrical conductivities on inductance and AC resistivity were performed on this model (Figures 33 and 34).
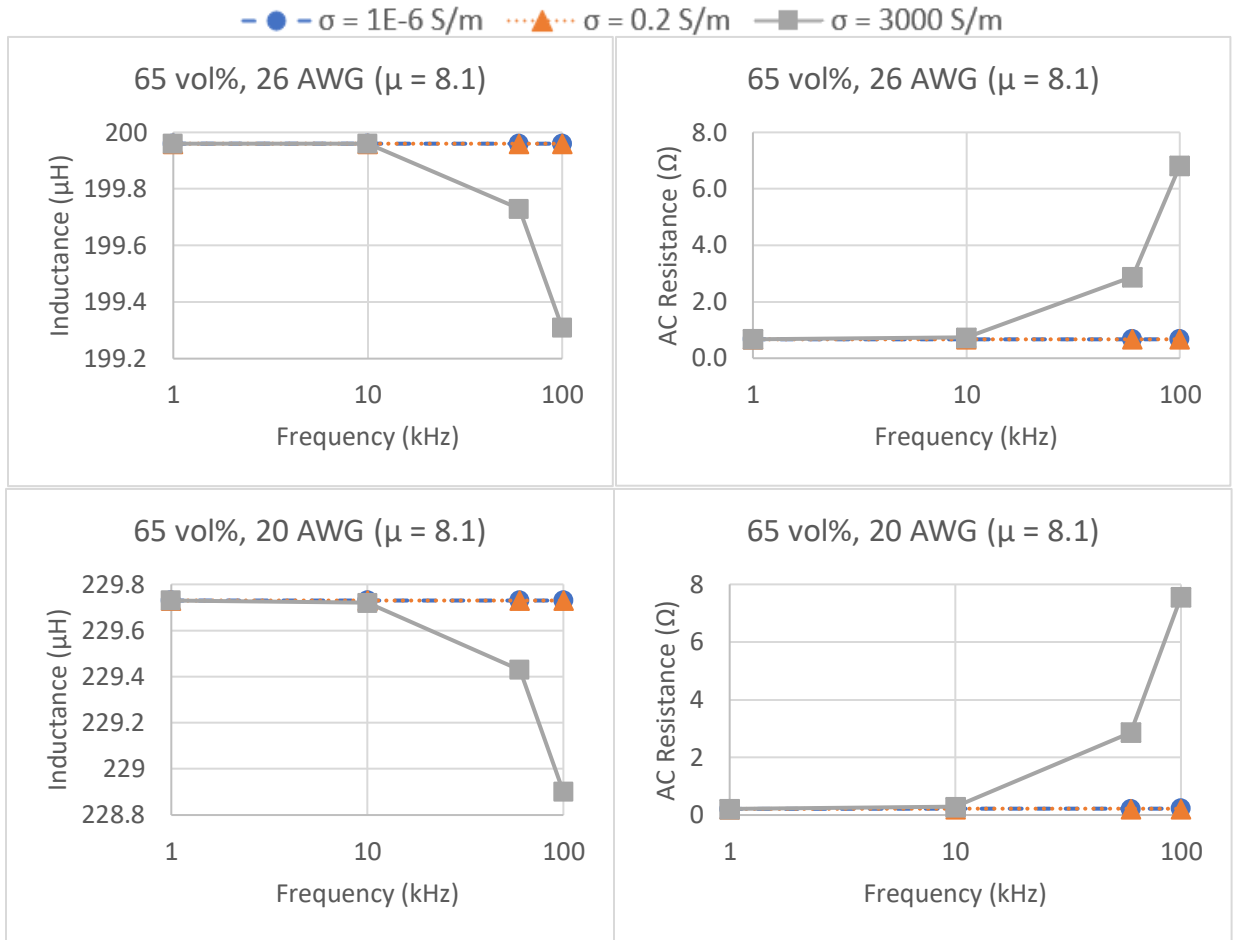
Figure 33. Effect of electrical conductivity on inductance and AC resistance results for 65 vol% model using μ = 8.1.
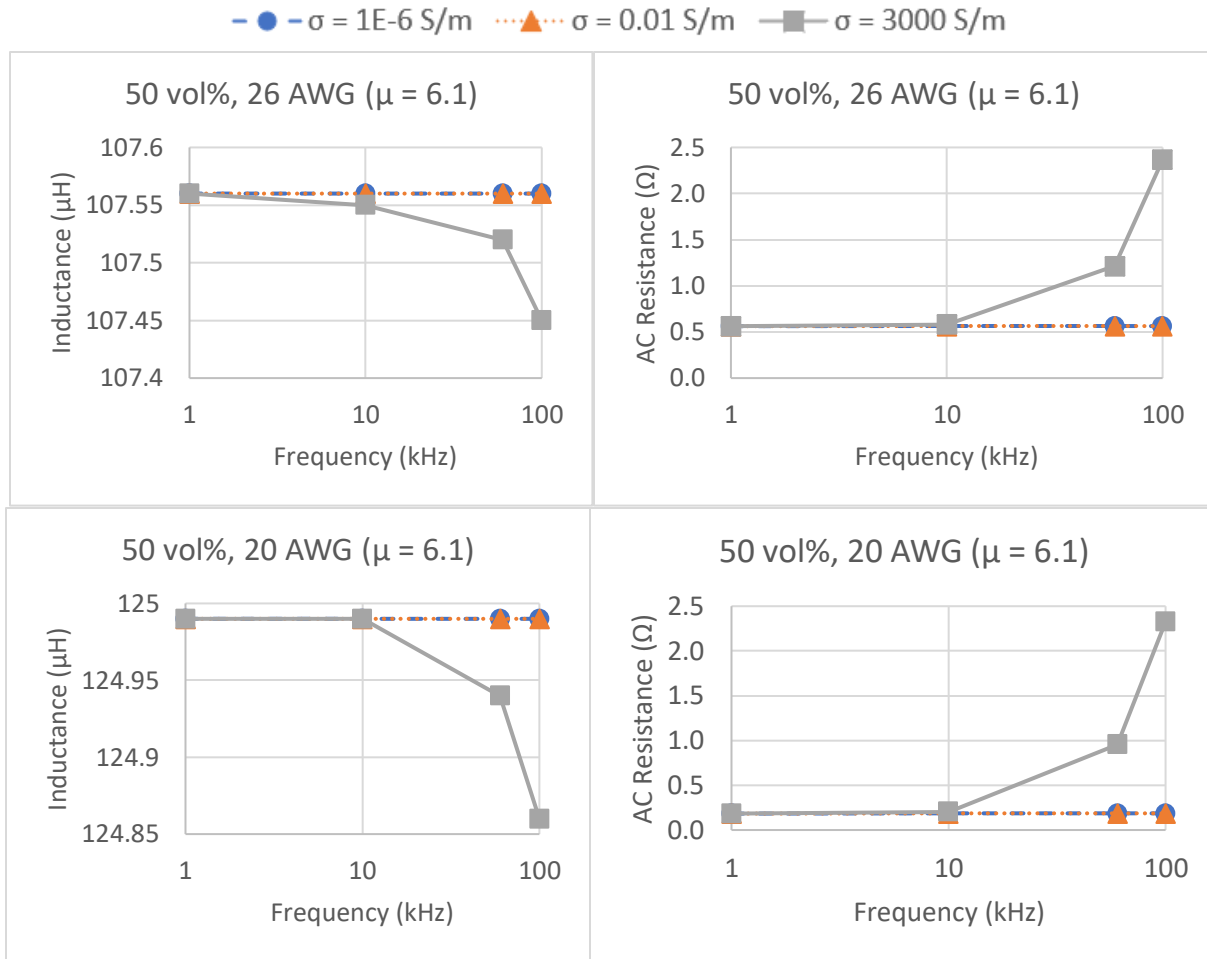
Figure 34. Effect of electrical conductivity on inductance and AC resistance results for 50 vol% model using μ = 6.1.

With the third model showing the same trends in frequency dependence of both inductance and AC resistance only at 3000 S/m, it suggests that using a higher electrical conductivity to model the core materials better captures core losses. However, the value of 3000 S/m does not match with the expected high resistivity of the IN SMC core, suggesting that either the electrical conductivities of the core materials made in this project are higher than expected in comparison to previous inductors, and/or that there is another mechanism(s) behind the large increase in measured AC resistance at 100 kHz that is not addressed by core conductivity, such as the skin effect in the copper wiring. This lowers the confidence level of the AC resistance results for all the models. In contrast, the permeabilities used in this model have a high confidence level because they are calculated directly from the experimental results and better reflect the permeabilities of the actual

prototypes. As such, the final model uses μ = 8.1 because of the high confidence level and low percent differences between experimental and simulated values of inductance.

4.3.6   Final Model for Simulation

The fourth and final model in the project confirmed the results seen in earlier models for inductance using μ = 8.1 and 6.1 and electrical conductivity σ = 3000 S/m to better represent the frequency dependence of the AC resistance results of the fabricated inductors. Highlighted values for 60 kHz from the model are compared to the interpolated values for the same frequency from the experimental results (Table 7) with the percent differences shown below. Percent difference in AC resistance values are not shown for 60 kHz because the experimental value was not interpolated at that frequency due to the nonlinear nature of the measured AC resistance.

Table 16 shows the smallest percent differences in inductance and AC resistivity among all the models, confirming the use of the calculated permeabilities and a high electrical conductivity value to increase accuracy and precision. The intention of changing the electrical conductivity of the core material was to match the slight drop in inductance that was seen at high frequencies in the experimental results. It should be noted that raising this conductivity value had no change on inductance at 1 kHz, likely because there is not the same mechanism(s) occurring at low frequencies, whether it is the skin effect or eddy current loss. In addition, the AC resistance matched more closely to the experimental frequency dependence with a range of 7% - 98% difference when a higher electrical conductivity was assumed for the core materials. The confidence level of the AC resistance results is low given that the actual electrical conductivities of the core materials are unknown and that there is the possibility of another mechanism(s) causing the drop in inductance at 100 kHz.

4.3.7   Discussion of Overall Results

The fourth model was chosen as the final model for simulation because the confidence level of the permeability values was the highest and the percent differences for both the inductance and AC resistance results was the lowest of all the models. The permeabilities used in the fourth model were calculated directly from the experimental inductance results, which resulted in low percent difference results within the acceptable range for simulations (where some percent difference between model and experiment remains because the fineness of the mesh is not sufficient to capture the exact behavior of the system). The first two sets of permeabilities used data from

previous IN SMC prototypes that were made with iron nitride powder from a different vendor used by Sandia, which may have higher inductance than the new iron nitride powder used in these prototypes.

Table 15. An adjusted core conductivity value of 3000 S/m shows a slight frequency – AC resistance relationship.

Model	Frequency (kHz)	Inductance (µH)	% Difference in Inductance	AC Resistance (Ω)	% Difference in AC Resistance
65 vol% 26 AWG ($\mu_r = 8.1$)	1	199.96	8%	0.6711	12%
	10	199.96	8%	0.7323	14%
	60	199.73	8%	2.8892	
	100	199.31	9%	6.814	7%
65 vol% 20 AWG ($\mu_r = 8.1$)	1	229.73	2%	0.21304	25%
	10	229.72	2%	0.2870	66%
	60	229.43	4%	2.8675	
	100	228.9	6%	7.559	98%
50 vol% 26 AWG ($\mu_r = 6.1$)	1	107.56	8%	0.5629	18%
	10	107.55	9%	0.58081	17%
	60	107.52	9%	1.2119	
	100	107.45	9%	2.3641	84%
50 vol% 20 AWG ($\mu_r = 6.1$)	1	124.99	4%	0.18338	27%
	10	124.99	5%	0.20488	40%
	60	124.94	6%	0.95611	
	100	124.86	7%	2.326	18%

Figures 29 - 34 show that permeability does not appear to impact AC resistance in the equations and physics used in the COMSOL™ simulation. However, the wide spread of the percent differences for the AC resistances in all four models indicates that a major mechanism(s) is likely

missing from the current model to predict the AC dependence on frequency accurately and precisely. Changing the electrical conductivity of the core had some effect with frequency, but it is probable that the large increase in AC resistance at 100 kHz is due to both the skin effect in the copper wiring and possibly the eddy currents in the core. With the current model, the skin effect is not accounted for due to restrictions in the winding geometry of the COMSOL^{TM} model. Since the electrical conductivity values of the core materials are currently unknown and the skin effect can't be included in homogenous turn models, the AC resistance results have low confidence among all the models.

As for the 50 vol%, 26 AWG inductor that consistently shows a low percent difference in AC resistance at 100 kHz, even changing the conductivity to 3000 S/m did not address the discrepancy. Since the original measurement of AC resistance in the prototype was lower than the others, this may be an erroneous reading or could be a result of lower eddy current losses due to the lower vol% loading. It is important to note that the AC resistance value for the 50 vol%, 20 AWG inductor was only about 2 Ω, which is not much larger than the value for the core wound with 26 AWG wiring. As such, these lower values and consequently lower percent differences seen in the models above may be a result of the core rather than the wiring as was initially assumed.

4.3   Combining Model and Experiment Results

The goal of the project was to produce a COMSOL^{TM} model that accurately and precisely reflects the inductance of the experimental prototypes. The percent differences for each sample's inductance results were calculated to determine the accuracy of the model. The similarity between the percent difference results reflects the precision of the model. The AC resistance results were not included in determining the accuracy and precision of the model as the level of confidence in the data used for electrical conductivity values was low.

As shown above, the fourth iteration of the model had the most accurate and precise results for inductance. Figure 35 compares the inductance results between the third model (calculated permeabilities) and the experimental prototypes. Figure 36 shows the discrepancies between the AC resistance results for the model and prototypes.
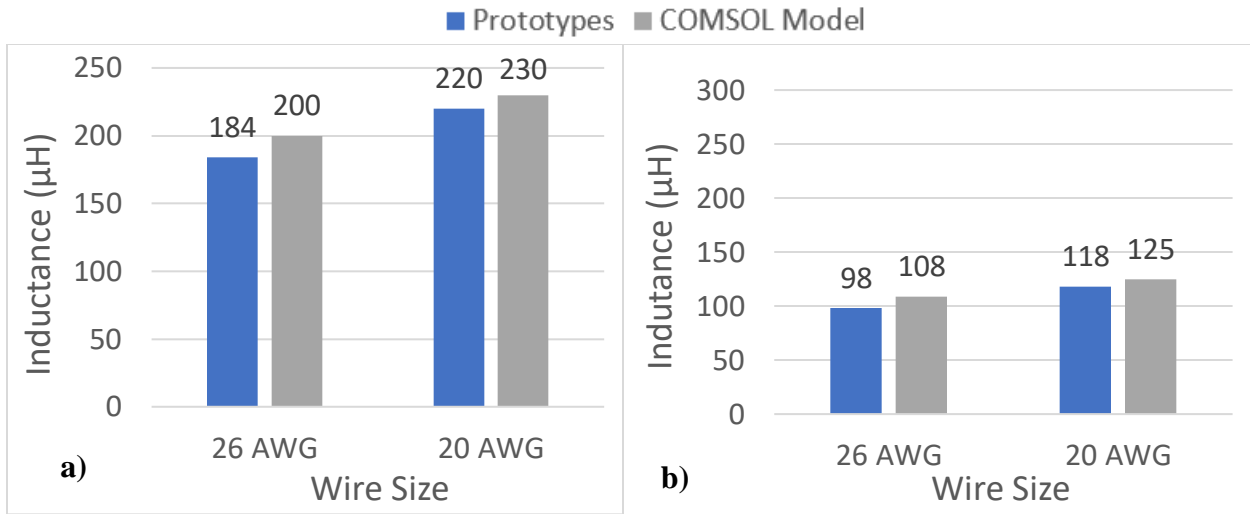
Figure 35. a) The inductance results from the 65 vol% inductors for both wire sizes, b) the inductance results for the 50 vol% inductors for both wire sizes.
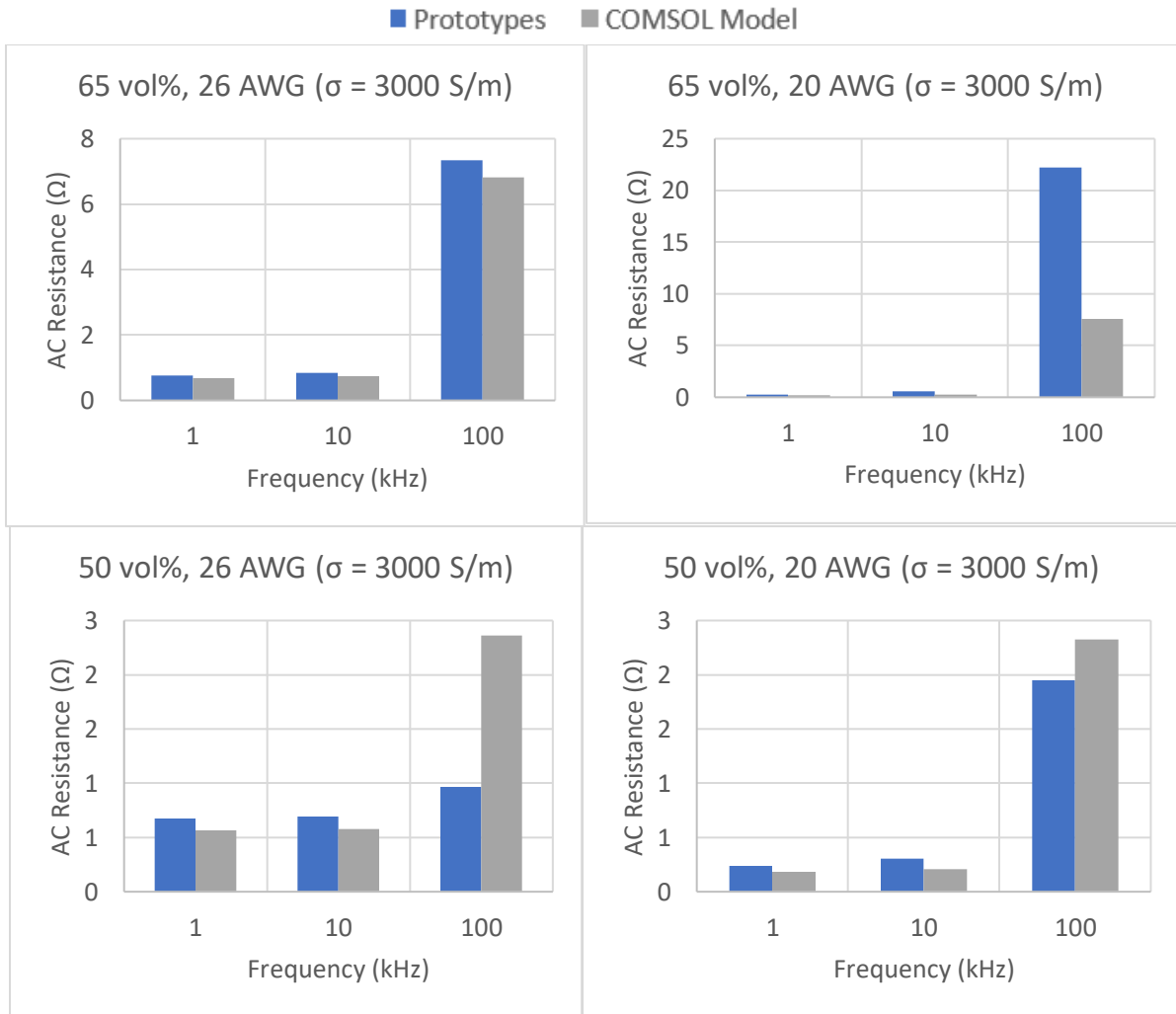
Figure 36. AC resistance results for all four inductors comparing experiment and model.

Visually, the inductance results from the fourth model closely match the experimental results. Figure 35 shows that the inductance of the model is always higher than that of the prototypes, which indicates that the model is likely not capturing core losses completely or accurately. Additionally, the inductance is higher for the 65 vol% cores than the 50 vol% cores in both the model and the experiment due to the increased loading of IN in the epoxy and corresponding increase in permeability. Inductance is also higher for cores wound with the 20 AWG wire because of the decreased AC resistance from the increased diameter of the wire. Finally, the highest inductance for both the model and the prototypes corresponds with the 65 vol% IN core wound with 20 AWG wire.

In contrast, the AC resistance results shown in Figure 36 indicate that the model does not completely account for the sharp increase in resistance at 100 kHz. This model error may be a result of the skin effect where the alternating current crowds towards the surface of the conductor, consequently decreasing the effective cross-sectional area of the wire and therefore increasing the resistance of the wire. At lower frequencies like 1 and 10 kHz, the model more accurately predicts the AC resistance but does not capture the resistivity of the prototypes accurately. This is true for both wire gauges for the 65 vol% core material. Interestingly, the 50 vol% cores exhibit a considerably smaller jump in AC resistance at high frequencies, which does not correlate with the assumption that the skin effect is dominating the AC resistance behavior. This could indicate that the main driver for the sharp increase in AC resistance is the electrical conductivity associated with the iron nitride loading in the core, rather than the thickness of wire. Thus, the higher AC resistances seen in the 65 vol% cores may have higher influence from core losses instead of or in addition to the skin effect. Further investigation into this phenomenon is recommended to determine why there is a sharp increase in AC resistance at high frequencies for 65 vol% inductors but not for the 50 vol% inductors. The results of the iterative analysis with varying electrical conductivities suggest that the core may not be as resistive as initially thought, as the lowest percent difference in AC resistance results between the experimental and model belonged to the model using an electrical conductivity of 3000 S/m. As such, there remains the possibility that the cores may have an electrical conductivity on the order of 10^3 S/m or even higher.

5   Conclusions and Future Work

5.1.   Fabrication and Experiment

The fabrication of the 4 prototypes indicates that higher vol% loading of iron gives a higher inductance for IN SMC inductors. Therefore, future work at Sandia should focus on improving the process for making 65 vol% IN samples and increasing the vol% IN loading. By comparing the 50 vol% to the 65 vol% inductors, it is seen that a large performance barrier at higher percent IN loading is due to the increase in voids. Sandia intends to use hot pressing to address this problem, achieving a denser composite overall. In addition, the uniformity of the distribution of IN powder in the epoxy matrix is still under investigation, so more information surrounding the distribution of iron nitride in the epoxy will be valuable in determining the effectiveness of higher vol% cores.

Limitations in our experiment during the mixing and molding process may warrant improvements to the lab equipment used. For example, the use of a Teflon beaker in mixing the 50 vol% material may result in less adhesion of the material to the beaker's surface, and therefore reduce the mass loss of the material during transfer into the mold. Additionally, the use of a shorter but wider container (such as a crystallizing dish instead of a beaker) would increase heat transfer to the material on the hot plate, and perhaps reduce the amount of material that adheres to the side of the mixing container during transfer to the mold.

As for the windings, the high temperature copper wiring performs well at 1 and 10 kHz but sees a steep increase in AC resistance at 100 kHz. This effect could warrant the use of wire alternatives, such as Litz wire. Litz wire performs better in the high frequency range by mitigating the skin effect and may keep the inductance more constant at high frequencies. Additionally, the data shown in this report indicates that for a given number of turns, thicker wire produces higher inductance due to the lower overall resistance. However, it is worth noting that a significantly higher number of turns can fit on the same geometry of core by using thinner wire, which has a much greater effect on inductance. In addition, the thinner wire can operate at much higher frequencies without being affected by the skin effect, although its overall resistance would be higher than for thick wiring.

Beyond the inductor design, another possible area of future research is studying the effects of temperature, cure time, and/or vol% loading of iron nitride on the mechanical properties of the inductor. If iron nitride inductors are to be used for an EV application, it may be important to have

mechanical property data to see how well it withstands vibrational loads and elevated temperatures.

5.2.   Modeling and Simulation

The COMSOL^{TM} model was developed to minimize the percent difference between the experimental results and the simulation results, and used the constitutive relationship $\mathbf{B} = \mu\mathbf{H}$, where permeability is the ratio between magnetic flux density ($\mathbf{B}$) and magnetic field intensity ($\mathbf{H}$). Using permeabilities calculated from the experimental results yielded the smallest percent differences, indicating the accuracy and precision of the permeability model for the four samples fabricated in this project. The magnitude of the percent differences for the inductance results (2% - 9%) shows that the model somewhat captured the core losses in the four inductors with the caveat of the small sample size used in the project. The similarity of the percent differences indicates that the model can consistently predict the inductance of the inductors, again with a caveat due to the small sample size.

5.2.1.   Accounting for Hysteresis Losses

While the percent differences suggest that the current model is more precise rather than accurate, the permeability values for the iron nitride SMC cores are significantly lower than expected in comparison to previous values from other cores. This is in part due to accounting for the effective vol% loading of iron nitride resulting from voids in the core material. The lower permeability values could also be a result of the iron nitride powder from Stanford Advanced Materials that were used in these prototypes, as these are the first IN SMC prototypes made of the powder from this new vendor. For future work, the permeabilities and B-H curves of SMC samples made with the new iron nitride powder should be measured directly using a B-H analyzer to provide input for use in COMSOL to increase confidence in the simulation results.

Other than permeability, the constitutive relation between $\mathbf{B}$ and $\mathbf{H}$ in COMSOL^{TM} can also be adjusted to use a B-H curve, which may better account for magnetization saturation at high frequencies. This method requires more initial work with the experimental data in cleaning up the B-H curve to keep it monotonic, as COMSOL^{TM} will only accept monotonic curves. Additionally, there are restrictions on using B-H curves in COMSOL^{TM}, where a full B-H curve cannot be used directly in a frequency-domain study. A possible solution is to use an effective B-H curve which only looks at a section of the curve that can be used in a frequency-domain study. Another solution

is to analyze the B-H curve in a stationary study to extract results for use in a frequency-domain study[29]. This methodology allows the stationary study to solve the partial differential equation (PDE) for the DC component at each node in the mesh, which speeds up the frequency-domain study step to extract the AC component. Additionally, a frequency-domain perturbation study should be used instead of a frequency-domain study to handle the non-symmetric matrices that result from the stationary study[29].

5.2.2. Accounting for Eddy Current Losses

As for the AC resistances for the model and the experiment, the model does not produce the same significant increase in AC resistance at high frequencies, indicating that it is not accounting for the mechanism(s) behind the increase at 100 kHz. As described throughout the Results section, the sharp increase may be due to either the skin effect and/or different electrical conductivities of the core. Future work should focus on determining the cause of the sharp increase in AC resistance at high frequencies using the model and/or experimental research.

If it does turn out that the skin effect is impacting the results, that mechanism could be incorporated into the model in a few different ways. One way to accomplish this is with a different geometry that allows the coil to be modeled as a single conductor to visualize the skin depth. To accomplish this, each turn of the coil must be modeled separately, whereas the model used in this project utilized the homogeneous multi-turn conductor in COMSOL™. Additionally, the model must use at least a Fine mesh if not an even finer mesh to fully capture the skin effect in the coil. This method increases the computational load by a substantial amount. Another way to account for the skin effect is to change the effective diameter and packing fraction of the wires in the homogeneous multi-turn conductor assumption in the physics of the model. This can bypass the need to model the windings as a single conductor but may be less accurate.

As for the electrical conductivity contribution to the AC resistance, any future work with adjusting this parameter in COMSOL™ should use an experimentally determined value for iron nitride SMC cores. This can be a complex and non-trivial measurement, as there are two components that must be measured. The first is the DC component of resistance. The method used to measure DC resistance in this project should be adjusted to capture the possibility of different electrical pathways through the inductor. As a 3D shape, it is nearly impossible to predict the electrically conductive paths through the inductor without a better understanding of the spatial

distribution of iron nitride particles in the epoxy matrix. This becomes even more complex when considering the implications of the DC resistance results and visual observations of the 50 vol% inductor cores that suggest that the iron nitride is not homogeneously distributed through the inductor and instead concentrated towards the bottom of the core. First steps in this direction for future work should be to explore the distribution of iron nitride in the epoxy matrix through scanning electron microscopy (SEM) or energy-dispersive X-ray spectroscopy (EDS) analysis to determine the composition and the homogeneity of the composition of the inductor core. As for the AC component of core resistance, this can only be measured under operating conditions where there is a large amount of AC current flowing through the windings. The true electrical conductivity of the core will change as a function of frequency, where higher frequencies have greater overall impedance due to the inductive reactance component. In addition, one could derive the electrical conductivity of the core specific to exact operating conditions and frequency by taking highly sensitive temperature measurements and quantifying the amount of heat created due to eddy currents.

5.3.   Optimized Inductor

Both the simulation and experimental results show that the highest inductance was achieved by combining the 65 vol% core with 20 AWG windings, as expected. The 65 vol% core has the highest inductance performance because of the increased loading of iron nitride and therefore improved magnetic performance. The 20 AWG windings performed the best because of the decreased AC resistance from the larger cross-sectional area of the wire.

Using the permeability for 65 vol% determined previously ($\mu_r = 8.1$) and the Excel solver developed earlier in the project, the size of the inductor and number of turns was found for an optimized inductor that reaches an inductance goal of 667 μH. The goal of 667 μH includes an 11% difference from the 600 μH goal to account for the percent differences seen in this project. Based on this goal, the results of the Excel solver are $h = 1.5$ cm, $a = 1$ cm, and $b = 4$ cm with two layers of windings to make up 150 turns. The final geometry is shown in Figure 37. The inductance can further be increased by adding additional windings in multiple layers.
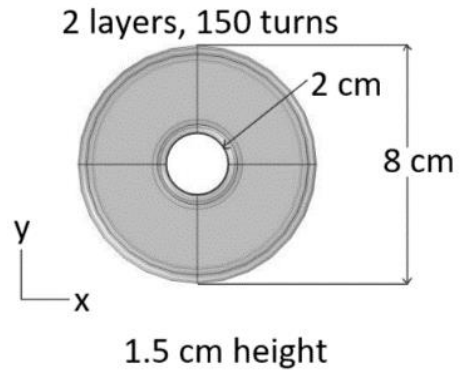
Figure 37. The optimized inductor is about 8 cm wide and 1.5 cm tall to fit 150 windings.

References

1. *Electric Vehicles – Analysis*. IEA. https://www.iea.org/reports/electric-vehicles (accessed Mar. 1, 2023).

2. Stevens, T. E.; Lewis, R.; Pearce, C. J.; Rodriguez, M. A.; Dickens, S.; McKenzie, B. B.; Atcitty, S.; Monson, T. *Synthesis and Magnetic Properties of Iron Nitrides.*; SAND2019-3592C; Sandia National Lab. (SNL-NM), Albuquerque, NM (United States), 2019.

3. James, L. Understanding the Role of Inductors in Power Electronics. *Power and Beyond* **2020**. https://www.power-and-beyond.com/understanding-the-role-of-inductors-in-power-electronics-a-dc947f2aa88d7ac3009791f798478d1c/ (accessed Nov. 12, 2022).

4. Elshimi, A. *Maxwell's equations: An intuitive view for engineers*. Power Electronics Tips. https://www.powerelectronictips.com/intuitive-view-of-maxwells-equations-faq/ (accessed Nov. 3, 2022).

5. 22.1 Magnetic Flux, Induction, and Faraday's Law. In *Induction, AC Circuits, and Electrical Technologies*; LibreTexts Physics; 2020. https://phys.libretexts.org/Bookshelves/University_Physics/Book%3A_Physics_(Boundless)/22%3A_Induction_AC_Circuits_and_Electrical_Technologies/22.1%3A_Magnetic_Flux_Induction_and_Faradays_Law (accessed Nov. 3, 2022).

6. TDK Global. *The Integral Role of Power Inductors in the Electrification of Cars*. Featured Stories - TDK Global. https://www.tdk.com/en/featured_stories/entry_050-Inductors-Electronic-Component-for-Automobiles.html (accessed Nov. 3, 2022).

7. Khan, M. A.; Ahmed, A.; Husain, I.; Sozer, Y.; Badawy, M. Performance Analysis of Bidirectional DC–DC Converters for Electric Vehicles. *IEEE Transactions on Industry Applications* **2015**, *51* (4), 3442–3452. https://doi.org/10.1109/TIA.2015.2388862 (accessed Nov. 4, 2022).

8. Al, M.; Van, J.; Gualous, H. DC/DC Converters for Electric Vehicles. In *Electric Vehicles - Modelling and Simulations*; Soylu, S., ed.; InTech, 2011. https://doi.org/10.5772/17048 (accessed Nov. 5, 2022).

9. Kazimierczuk, M. Fundamentals of Magnetic Devices. In *High Frequency Magnetic Components*; John Wiley & Sons, Inc., 2013; pp 1–80.

10. *Toroidal Transformer: What Is It? How Does It Work? Toroids*. Industrial Quick Search. https://www.iqsdirectory.com/articles/electric-transformer/toroidal-transformer.html (accessed Nov. 6, 2022).

11. Sen, P. C. *Principles of Electric Machines and Power Electronics*, Third Edition.; John Wiley & Sons, Inc., 2014; pp 618.

12. Horizon Technology. What Is Soft Magnetic Composite? | AC Motor Design. https://www.horizontechnology.biz/blog/soft-magnetic-composite-what-is (accessed Nov. 26, 2022).

13. Magnetic Materials: Soft Magnets. *University of Birmingham*. https://www.birmingham.ac.uk/Documents/college-eps/metallurgy/research/Magnetic-

Materials-Background/Magnetic-Materials-Background-10-Soft-Magnets.pdf (accessed Mar. 10, 2023).

14. Nave, C. *Hysteresis in magnetic materials*. http://hyperphysics.phy-astr.gsu.edu/hbase/Solids/hyst.html#c2 (accessed Nov. 26, 2022).

15. Nisticò, R.; Cesano, F.; Garello, F. Magnetic Materials and Systems: Domain Structure Visualization and Other Characterization Techniques for the Application in the Materials Science and Biomedicine. *Inorganics* **2020**, *8* (1), 6. https://doi.org/10.3390/inorganics8010006 (accessed Nov. 26, 2022).

16. Svensson, L.; Frogner, K.; Jeppsson, P.; Cedell, T.; Andersson, M. Soft Magnetic Moldable Composites: Properties and Applications. *Journal of Magnetism and Magnetic Materials* **2012**, *324* (18), 2717–2722. https://doi.org/10.1016/j.jmmm.2012.03.049 (accessed Nov. 26, 2022).

17. Nave, C. *Permanent Magnets*. HyperPhysics. http://hyperphysics.phy-astr.gsu.edu/hbase/Solids/magperm.html#c1 (accessed Nov. 26, 2022).

18. Hanejko, F. *Soft Magnetic Composites and Permeability*. Horizon Technology. https://www.horizontechnology.biz/blog/soft-magnetic-composites-and-permeability (accessed Nov. 26, 2022).

19. Kuphaldt, T. Inductor Quirks. In *Alternating Current (AC)*; Lessons in Electrical Circuits; Design Science; Vol. 2. https://www.allaboutcircuits.com/textbook/alternating-current/chpt-3/inductor-quirks/ (accessed Nov. 25, 2022).

20. Princeton University. Eddy Currents. *The McGraw Center for Teaching and Learning*. https://commons.princeton.edu/motorcycledesign/wp-content/uploads/sites/70/2018/06/eddy_wiki.pdf (accessed Mar. 10, 2023).

21. Rommel, D. P.; Di Maio, D.; Tinga, T. Transformer Hot Spot Temperature Prediction Based on Basic Operator Information. *International Journal of Electrical Power & Energy Systems* **2021**, *124*. https://doi.org/10.1016/j.ijepes.2020.106340 (accessed Nov. 26, 2022).

22. Lupu, N. Magnetostriction vs. Magnetoelastic Effects. European School on Magnetism, Cluj-Napoca, Romania, Sep 9-18, 2007. https://magnetism.eu/esm/2007-cluj/questions/magnetostriction.pdf (accessed Mar. 10, 2023).

23. Magnetic Models. *Magnetostrictive Hysteresis Loop of Mn-Zn Ferrite for Power Applications Measured by Semiconductor Strain Gauges*; Wikimedia Commons, 2014. https://commons.wikimedia.org/w/index.php?curid=34164668 (accessed Mar 10, 2023).

24. Power & Energy Engineering Team. *Inductor Reference Guide*; Abracon, 2020. https://abracon.com/uploads/resources/Abracon-Inductor-Reference-Guide.pdf (accessed Nov. 25, 2022).

25. Hanejko, F. *Core & Hysteresis Loss in Induction Motors: Lamination vs. SMC*. Horizon Technology. https://www.horizontechnology.biz/blog/hysteresis-core-loss-in-induction-motors-smc-steel-lamination (accessed Nov. 12, 2022).

26. Sandia National Labs. *R&D 100 Winner 2022: Iron Nitride Soft Magnetics*. YouTube. https://www.youtube.com/watch?v=20KtRwJBcWg (accessed Dec. 1, 2022).

27. Monson, T.; Stevens, T.; Pearce, C.; Hoyt, M.; Vreeland, E.; Delaney, R.; Atcitty, S. *New Iron Nitride Soft Magnetic Components*; SAND2021-0511C; Sandia National Laboratories: OSTI.gov (accessed Mar. 3, 2023).

28. *14.3: Self-Inductance and Inductors*. Physics LibreTexts. https://phys.libretexts.org/Bookshelves/University_Physics/Book%3A_University_Physics_(OpenStax)/Book%3A_University_Physics_II_-_Thermodynamics_Electricity_and_Magnetism_(OpenStax)/14%3A_Inductance/14.03%3A_Self-Inductance_and_Inductors (accessed Nov. 6, 2022).

29. Langlois, E.; Monson, T. *Finite Element Modeling of Nanoscale-Enabled Microinductors for Power Electronics*; SAND2018-4159J; Sandia National Labs: Center for Integrated Nanotechnologies, 2018; pp 1–26 (accessed June 8, 2023).

Appendices

Appendix A: COMSOL^{TM} Model Detailed Report

The full report is only included for the 65 vol%, 26 AWG model due to the length of the report generated in COMSOL^{TM}. Following the full report, the parameters, materials, and results are shown for the other models as those are the only changes between each model.

65 vol%, 26 AWG Model
1.1 Parameters

PARAMETERS 1

Name	Expression	Value	Description
core_w	7.96 [mm]	0.00796 m	core width
core_ht	9.44 [mm]	0.00944 m	core height
core_cnt_rad	core_w/2 + 10.04 [mm]	0.01402 m	Core center radius
k	.69	0.69	packing factor
wire_dia	0.0159 [in]	4.0386E−4 m	
n_lay	1	1	# of coil layers
N_pl	floor((2*pi*core_cnt_rad*k)/(wire_dia))	150	Number of turns per layer
N	n_lay*N_pl	150	total number of turns
coil_thk	wire_dia*n_lay/k	5.853E−4 m	Coil thickness
coil_outer_w	core_w + coil_thk	0.0085453 m	Outer width with coil
coil_outer_ht	core_ht + coil_thk	0.010025 m	Outer height with coil
fil_rad_core	core_w/10	7.96E−4 m	core edge fillet radius

1.2 Materials

1.2.1 Air
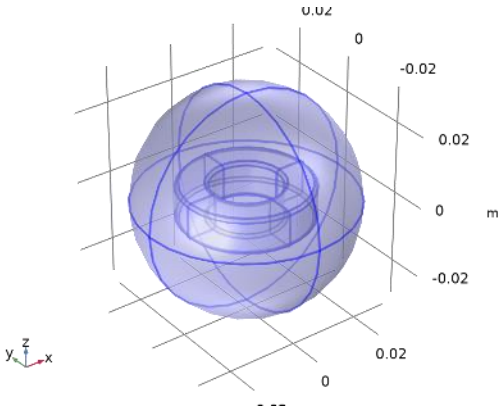
Air

MATERIAL PARAMETERS

Name	Value	Unit	Property group
Relative permeability	1	1	Basic
Relative permittivity	1	1	Basic
Electrical conductivity	0	S/m	Basic

BASIC

Description	Value	Unit
Relative permeability	1	1
Relative permittivity	1	1
Electrical conductivity	0	S/m

1.2.2 Copper
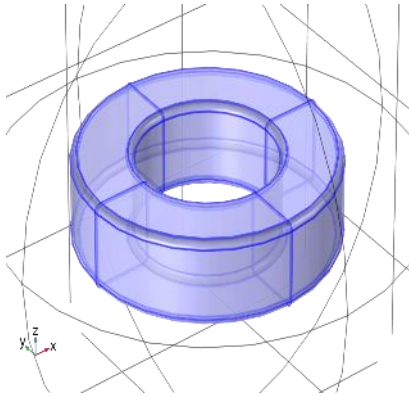
Copper

Geometric entity level   Domain

Selection   Geometry geom1: Dimension 3: Domain 2

MATERIAL PARAMETERS

Name	Value	Unit	Property group
Relative permeability	1	1	Basic
Relative permittivity	1	1	Basic

BASIC

Description	Value
Relative permeability	1
Relative permittivity	1

1.2.3 Material 3-core
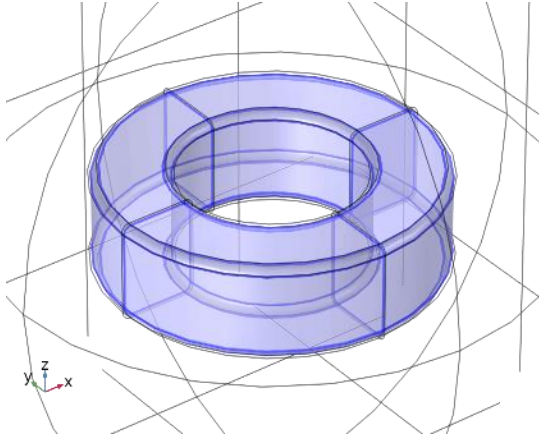
Material 3-core

Geometric entity level	Domain
Selection	Geometry geom1: Dimension 3: Domain 3

MATERIAL PARAMETERS

Name	Value	Unit	Property group
Relative permeability	8.1	1	Basic
Relative permittivity	1	1	Basic
Electrical conductivity	1E-6	S/m	Basic

BASIC

Description	Value	Unit
Relative permeability	8.1	1
Relative permittivity	1	1
Electrical conductivity	1E-6	S/m

1.3 Magnetic Fields

USED PRODUCTS

AC/DC Module

COMSOL Multiphysics
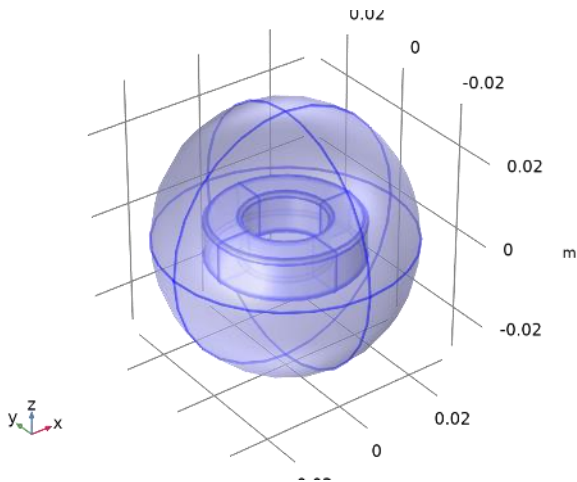
Magnetic Fields

Geometric entity level	Domain
Selection	Geometry geom1: Dimension 3: All domains

EQUATIONS

$$\nabla \times \mathbf{H} = \mathbf{J}$$
$$\mathbf{B} = \nabla \times \mathbf{A}$$
$$\mathbf{J} = \sigma \mathbf{E} + j\omega \mathbf{D} + \mathbf{J}_e$$
$$\mathbf{E} = -j\omega \mathbf{A}$$

1.3.1 Ampère's Law 1
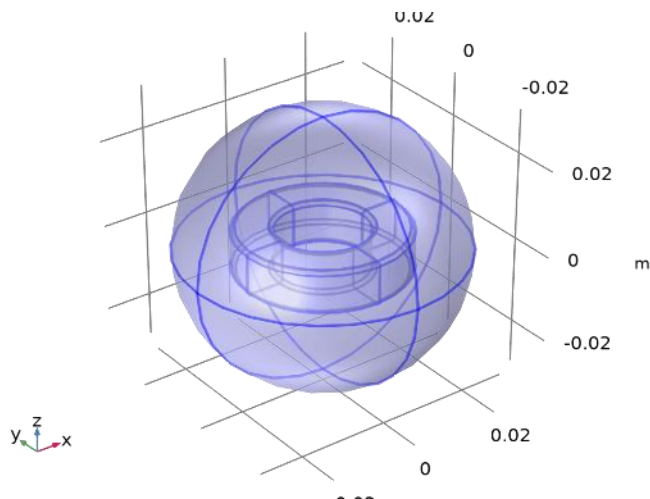
Ampère's Law 1

SELECTION

70

Geometric entity level   Domain

Selection   Geometry geom1: Dimension 3: All domains

EQUATIONS

$$\mathbf{E} = -j\omega\mathbf{A}$$
$$\nabla \times \mathbf{H} = \mathbf{J}$$
$$\mathbf{B} = \nabla \times \mathbf{A}$$
$$\mathbf{J} = \sigma\mathbf{E} + j\omega\mathbf{D}$$

Constitutive Relation B-H

SETTINGS

Description	Value
Magnetization model	Relative permeability
Relative permeability	From material

Constitutive Relation Jc-E

SETTINGS

Description	Value
Conduction model	Electrical conductivity
Electrical conductivity	From material

Constitutive Relation D-E

SETTINGS

Description	Value
Relative permittivity	From material

Coordinate System Selection

SETTINGS

Description	Value
Coordinate system	Global coordinate system

1.3.2 Magnetic Insulation 1
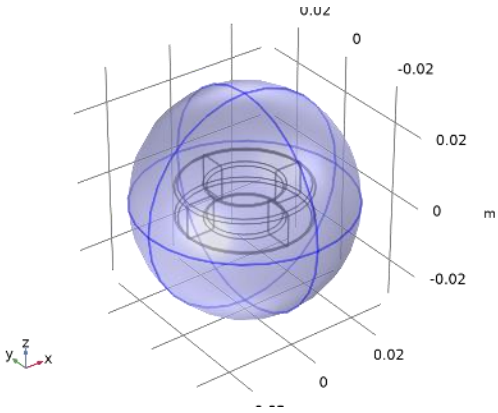
Geometric entity level	Boundary
Selection	Geometry geom1: Dimension 2: All boundaries

EQUATIONS

$$n \times A = 0$$

1.3.3 Initial Values 1
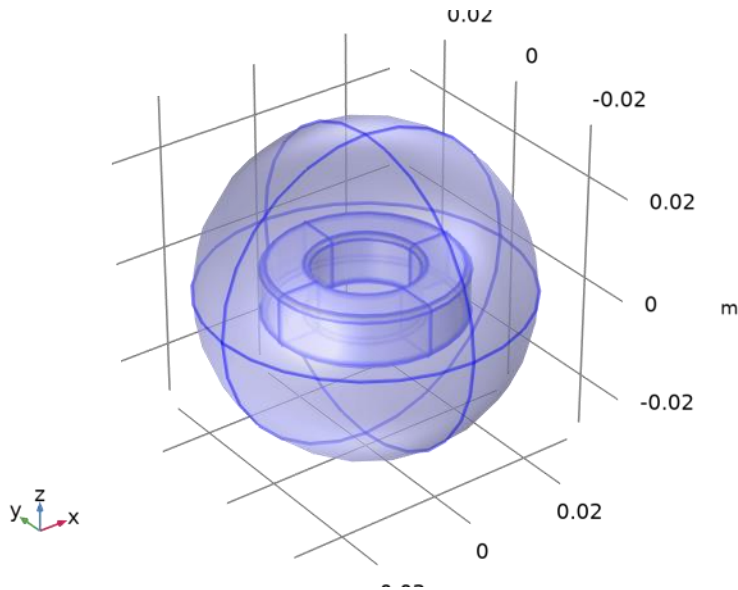
SELECTION

Geometric entity level	Domain
Selection	Geometry geom1: Dimension 3: All domains

SETTINGS

72

Description	Value	Unit
Magnetic vector potential	{0, 0, 0}	Wb/m

Coordinate System Selection

SETTINGS

Description	Value
Coordinate system	Global coordinate system

1.3.4 Coil 1
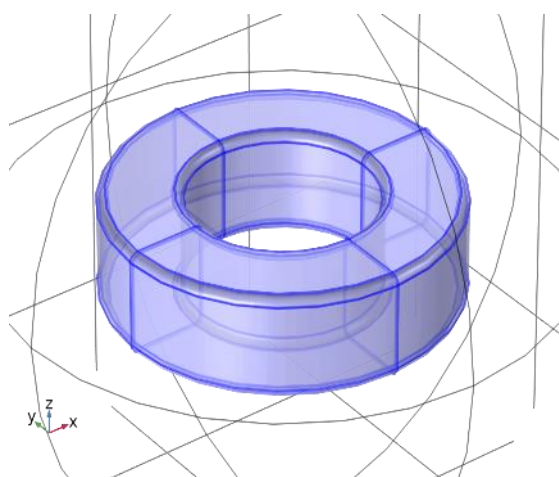
SELECTION

Geometric entity level	Domain
Selection	Geometry geom1: Dimension 3: Domain 2

EQUATIONS

$$\mathbf{J}_e = \frac{NI_{coil}}{A}\mathbf{e}_{coil}$$

Coil

SETTINGS

Description	Value	Unit
Coil name	1	
Conductor model	Homogenized multiturn	
Coil type	Numeric	
Coil excitation	Current	

Description	Value	Unit
Coil current	1	A

Homogenized Multiturn Conductor

SETTINGS

Description	Value	Unit
Number of turns	N	
Coil wire conductivity	6E7	S/m
Coil wire cross-section area	From round wire diameter	
Coil wire diameter	wire_dia	m

Constitutive Relation B-H

SETTINGS

Description	Value
Magnetization model	Relative permeability
Relative permeability	From material

Constitutive Relation D-E

SETTINGS

Description	Value
Relative permittivity	From material

Coordinate System Selection

SETTINGS

Description	Value
Coordinate system	Global coordinate system

PROPERTIES FROM MATERIAL

Property	Material	Property group
Relative permeability	Copper	Basic
Relative permittivity	Copper	Basic

1.3.5 Geometry Analysis 1
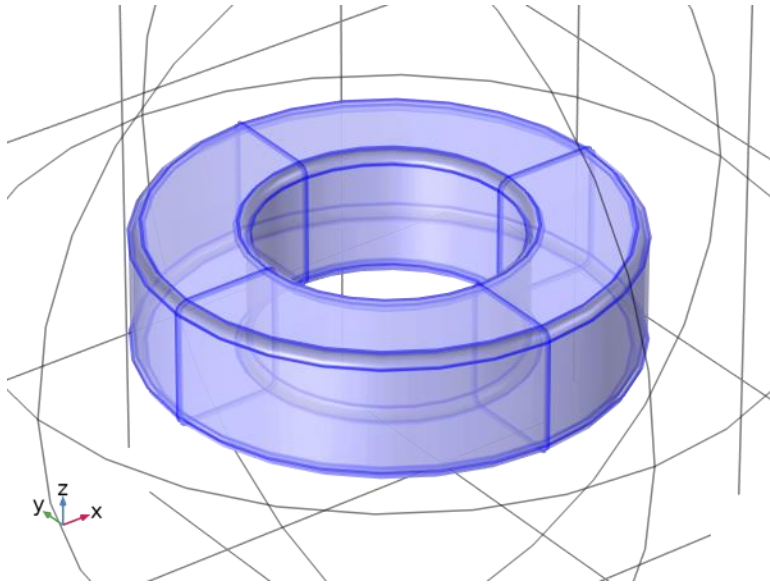
Geometry Analysis 1

Geometric entity level	Domain
Selection	Geometry geom1: Dimension 3: All domains

Coil Geometry

SETTINGS

Description	Value
Coil length multiplication factor	1
Coil area multiplication factor	1

1.3.6 Input 1
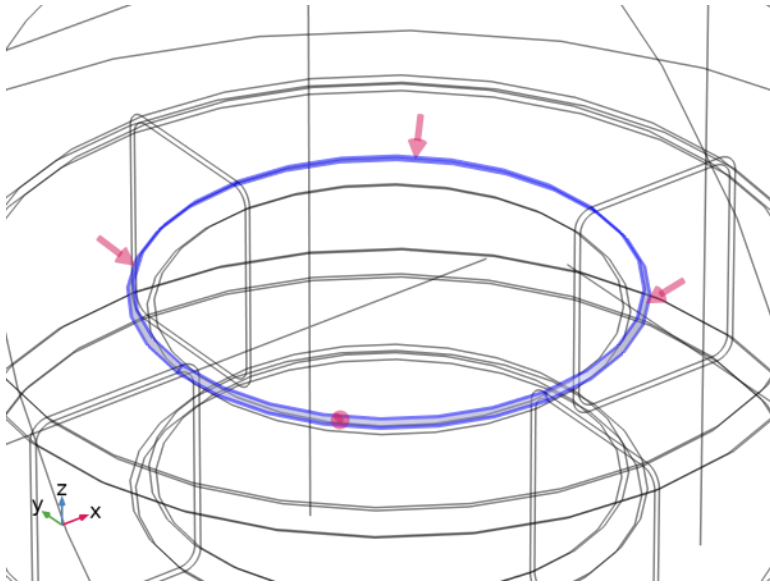
Input 1

Geometric entity level	Boundary
Selection	Geometry geom1: Dimension 2: Boundaries 27–28, 52, 67

Loss Calculation 1
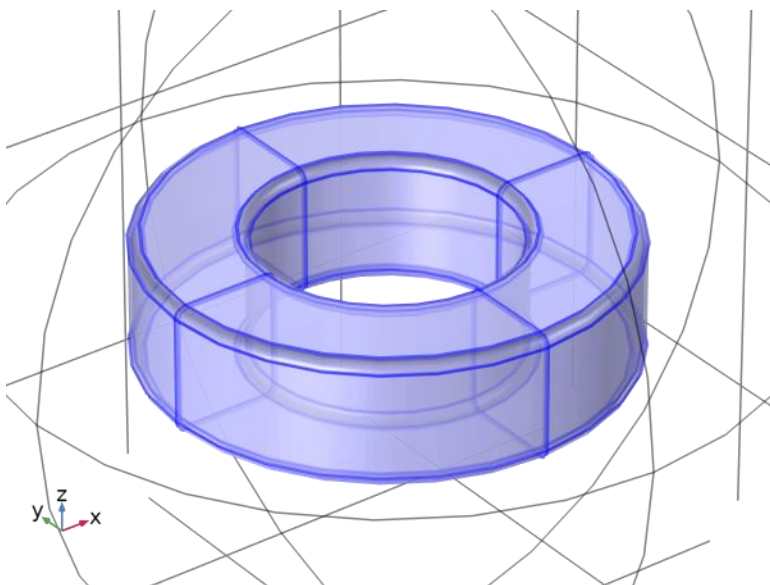
Loss Calculation 1

Geometric entity level	Domain

Selection   Geometry geom1: Dimension 3: All domains

EQUATIONS

$$Q = \frac{1}{T}\int_{T_{end}-T}^{T_{end}} \mathbf{J}\cdot\mathbf{E}\, dt$$

Loss Model

SETTINGS

Description	Value
Loss model	From resistive heating

1.3.7 Ampère's Law 2
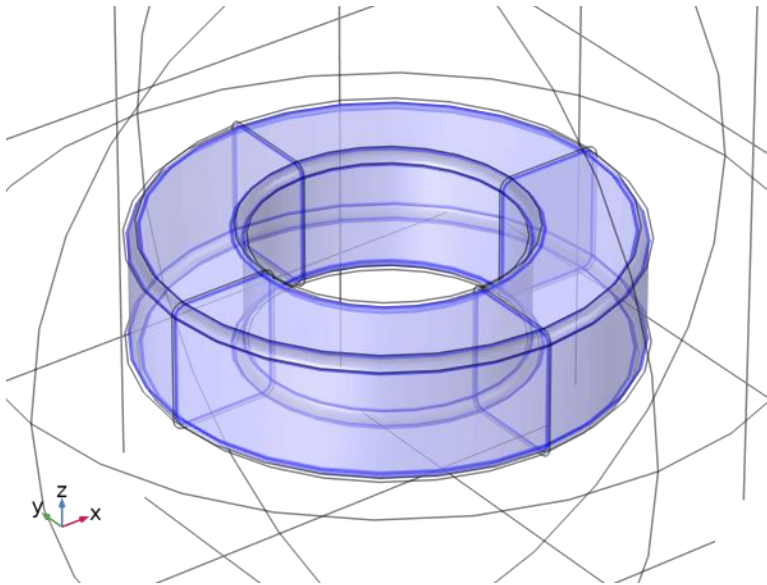
Ampère's Law 2

SELECTION

Geometric entity level	Domain

Selection   Geometry geom1: Dimension 3: Domain 3

EQUATIONS

$$\nabla \times \mathbf{H} = \mathbf{J}$$
$$\mathbf{B} = \nabla \times \mathbf{A}$$
$$\mathbf{J} = \sigma\mathbf{E}$$

Constitutive Relation B-H

SETTINGS

Description	Value
Magnetization model	Relative permeability
Relative permeability	From material

Constitutive Relation Jc-E

SETTINGS

Description	Value
Conduction model	Electrical conductivity
Electrical conductivity	From material

Constitutive Relation D-E

SETTINGS

Description	Value
Relative permittivity	From material

Coordinate System Selection

SETTINGS

Description	Value
Coordinate system	Global coordinate system

PROPERTIES FROM MATERIAL

Property	Material	Property group
Relative permeability	Material 3-core	Basic
Electrical conductivity	Material 3-core	Basic
Relative permittivity	Material 3-core	Basic

1.3.8 Gauge Fixing for A-field 1
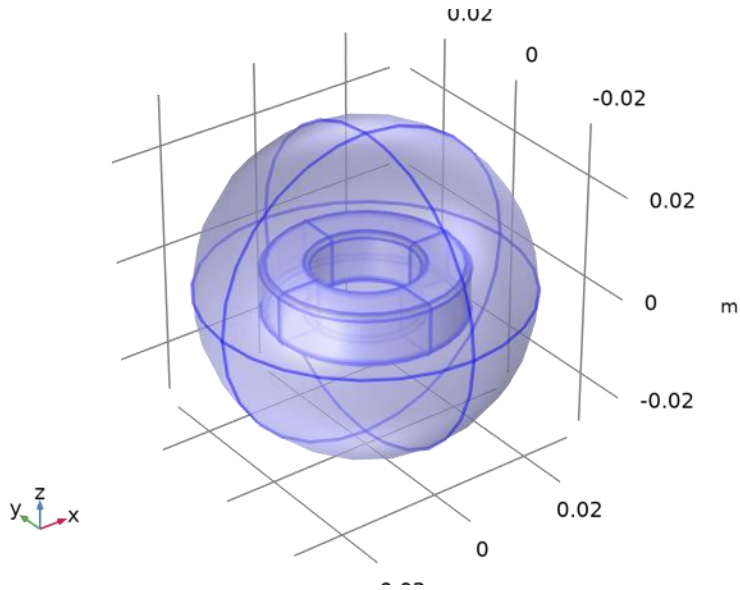
Gauge Fixing for A-field 1

Geometric entity level	Domain
Selection	Geometry geom1: Dimension 3: All domains

EQUATIONS

$$\nabla \cdot \mathbf{A} = 0$$

Gauge Fixing for A-field

SETTINGS

Description	Value	Unit
Equation form	Study controlled	
Divergence condition variable scaling	1	A/m

1.4 Mesh
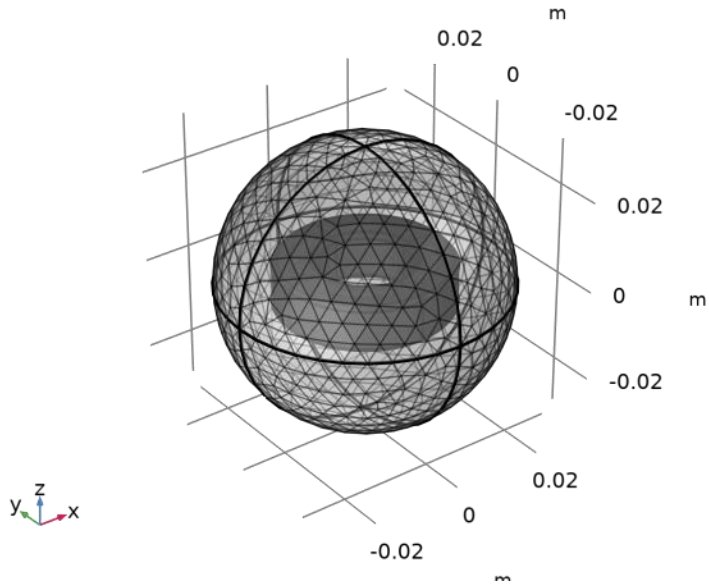
Mesh 1

SETTINGS

Description	Value
Maximum element size	0.0048
Minimum element size	6E-4
Curvature factor	0.5
Resolution of narrow regions	0.6
Maximum element growth rate	1.45
Predefined size	Fine
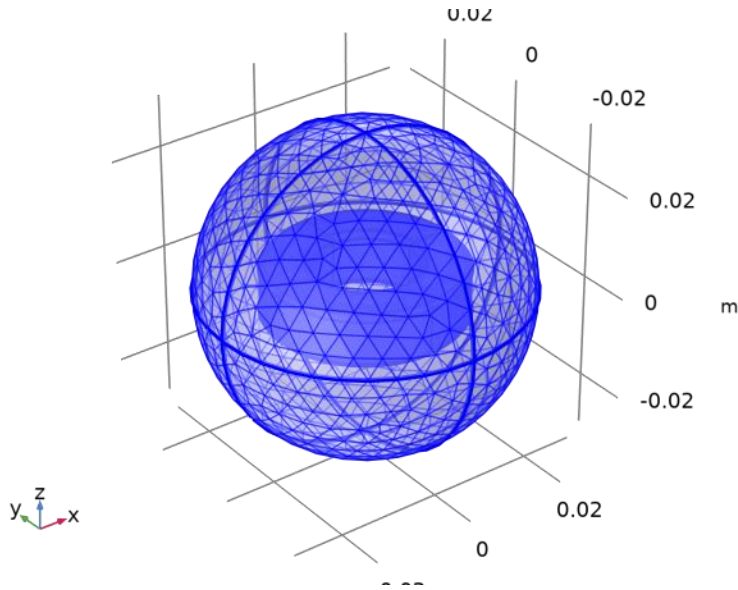
1.5 Study

1.5.1 Coil Geometry Analysis

STUDY SETTINGS

Description	Value
Include geometric nonlinearity	Off

PHYSICS AND VARIABLES SELECTION

Physics interface	Solve for	Equation form
Magnetic Fields (mf)	On	Automatic (Coil geometry analysis)

MESH SELECTION

Component	Mesh
Component 1	Mesh 1

1.5.2 Frequency Domain

Frequencies (kHz)
1,10,60,100

STUDY SETTINGS

Description	Value
Include geometric nonlinearity	Off

STUDY SETTINGS

Description	Value
Frequency unit	kHz

SETTINGS

Description	Value
Frequencies	{1, 10, 60, 100}

PHYSICS AND VARIABLES SELECTION

Physics interface	Solve for	Equation form
Magnetic Fields (mf)	On	Automatic (Frequency domain)

MESH SELECTION

Component	Mesh
Component 1	Mesh 1

1.6 Results

1.6.1 Study 1/Solution 1

SOLUTION

Description	Value
Solution	Solution 1
Component	Component 1 (comp1)
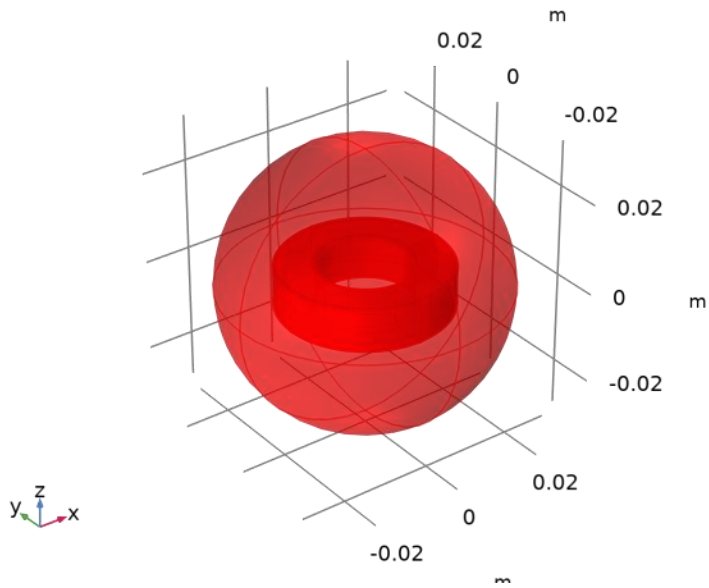
Dataset: Study 1/Solution 1

1.6.2 Tables

Global Evaluation 1

freq (kHz)	Coil inductance (uH)	Coil resistance (AC) (Ω)
1	199.96	0.67049
10	199.96	0.67058
60	199.96	0.67113
100	199.96	0.67157

1.6.3 Magnetic Flux Density Norm (mf)

freq(3)=60 kHz Multislice: Magnetic flux density norm (T)
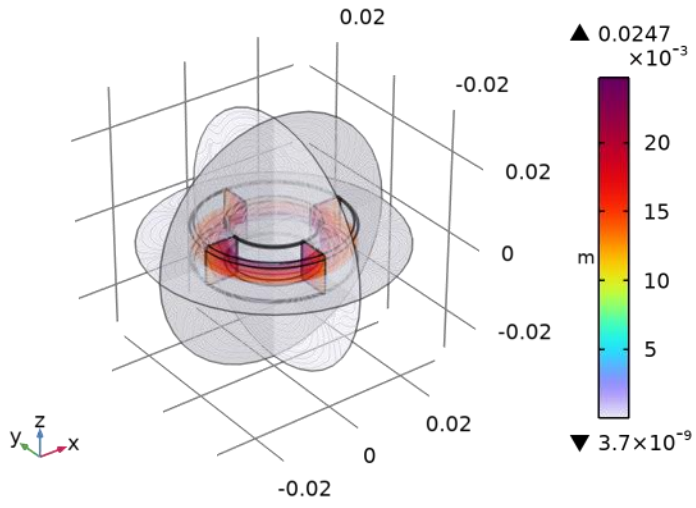
Multislice: Magnetic flux density norm (T)

65 vol%, 20 AWG

Name	Expression	Value	Description
core_w	7.929 [mm]	0.007929 m	core width
core_ht	10.324 [mm]	0.010324 m	core height
core_cnt_rad	core_w/2 + 9.948 [mm]	0.013913 m	Core center radius
k	.47	0.47	packing factor
wire_dia	.8128 [mm]	8.128E−4 m	
n_lay	3	3	# of coil layers
N_pl	floor((2*pi*core_cnt_rad*k)/(wire_dia))	50	Number of turns per layer
N	n_lay*N_pl	150	total number of turns
coil_thk	wire_dia*n_lay/k	0.0051881 m	Coil thickness
coil_outer_w	core_w + coil_thk	0.013117 m	Outer width with coil
coil_outer_ht	core_ht + coil_thk	0.015512 m	Outer height with coil
fil_rad_core	core_w/10	7.929E−4 m	core edge fillet radius
fil_rad_coil	coil_outer_w/10	0.0013117 m	coil edge fillet radius

Name	Value	Unit	Property group
Relative permeability	8.1	1	Basic
Relative permittivity	1	1	Basic
Electrical conductivity	1E-6	S/m	Basic

Global Evaluation 1

freq (kHz)	Coil inductance (uH)	Coil resistance (AC) (Ω)
1	229.73	0.2123
10	229.73	0.21285

freq (kHz)	Coil inductance (uH)	Coil resistance (AC) (Ω)
60	229.73	0.2159
100	229.73	0.21834
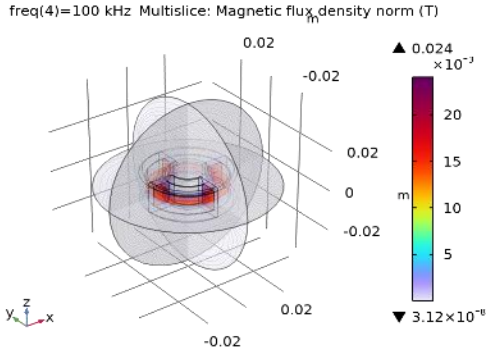
Multislice: Magnetic flux density norm (T)

50 vol%, 26 AWG

PARAMETERS 1

Name	Expression	Value	Description
core_w	7.98 [mm]	0.00798 m	core width
core_ht	6.76 [mm]	0.00676 m	core height
core_cnt_rad	core_w/2 + 9.9 [mm]	0.01389 m	Core center radius
k	.695	0.695	packing factor
wire_dia	.0159 [in]	4.0386E−4 m	
n_lay	1	1	# of coil layers
N_pl	floor((2*pi*core_cnt_rad*k)/(wire_dia))	150	Number of turns per layer
N	n_lay*N_pl	150	total number of turns
coil_thk	wire_dia*n_lay/k	5.8109E−4 m	Coil thickness
coil_outer_w	core_w + coil_thk	0.0085611 m	Outer width with coil
coil_outer_ht	core_ht + coil_thk	0.0073411 m	Outer height with coil
fil_rad_core	core_w/10	7.98E−4 m	core edge fillet radius
fil_rad_coil	coil_outer_w/10	8.5611E−4 m	coil edge fillet radius

Name	Value	Unit	Property group
Relative permeability	6.1	1	Basic
Relative permittivity	1	1	Basic
Electrical conductivity	1E-6	S/m	Basic

Global Evaluation 1

freq (kHz)	Coil inductance (uH)	Coil resistance (AC) (Ω)
1	109.09	0.5665
10	109.09	0.56655
60	109.09	0.56682
100	109.09	0.56704

freq(3)=60 kHz Multislice: Magnetic flux density norm (T)
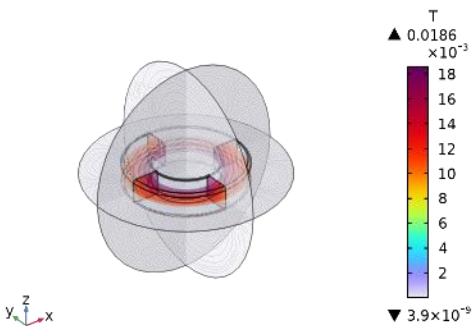
Multislice: Magnetic flux density norm (T)

50 vol%, 20 AWG

PARAMETERS 1

Name	Expression	Value	Description
core_w	7.958[mm]	0.007958 m	core width
core_ht	7.278 [mm]	0.007278 m	core height
core_cnt_rad	core_w/2 + 9.993 [mm]	0.013972 m	Core center radius
k	.47	0.47	packing factor

Name	Expression	Value	Description
wire_dia	.8128 [mm]	8.128E−4 m	
n_lay	3	3	# of coil layers
N_pl	floor((2*pi*core_cnt_rad*k)/(wire_dia))	50	Number of turns per layer
N	n_lay*N_pl	150	total number of turns
coil_thk	wire_dia*n_lay/k	0.0051881 m	Coil thickness
coil_outer_w	core_w + coil_thk	0.013146 m	Outer width with coil
coil_outer_ht	core_ht + coil_thk	0.012466 m	Outer height with coil
fil_rad_core	core_w/10	7.958E−4 m	core edge fillet radius
fil_rad_coil	coil_outer_w/10	0.0013146 m	coil edge fillet radius

MATERIAL PARAMETERS

Name	Value	Unit	Property group
Relative permeability	6.1	1	Basic
Relative permittivity	1	1	Basic
Electrical conductivity	1E-6	S/m	Basic

Global Evaluation 1

freq (kHz)	Coil inductance (uH)	Coil resistance (AC) (Ω)
1	124.99	0.18316
10	124.99	0.18342
60	124.99	0.18486
100	124.99	0.18601

freq(3)=60 kHz Multislice: Magnetic flux density norm (T)
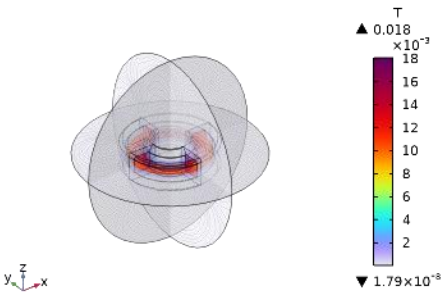
Multislice: Magnetic flux density norm (T)

Appendix B: Experimental Procedure for Inductor Fabrication

PPE

Persons performing the procedure described below should don the following PPE before beginning the procedure:

- Wear clothing that completely covers them from the chest to the toes, including closed-toe shoes
- Lab coat
- Gloves
- Safety glasses with side shielding
- Heat resistant gloves (able to withstand at least 180°C)

Please also tie back long hair and either remove or safely tuck away any dangling items such as necklaces, bracelets, hoodie strings, etc.

Section 1: Waste Management

We are in the process of organizing waste streams with EH&S with the below expected waste streams:

- Solid (powder) 4-AS and IN waste with expected amounts of < 1 g and solid waste of KimWipes, paper towels, and plastic weigh boats from step 3.1.14.
- Solid NND waste with disposable beaker/cup and micropipette tips from step 3.1.15.
- Liquid NND waste of NND dissolved in acetone and acetone used to clean NND from second paragraph of section 3.4. Expected amounts of < 3 mL.
- Liquid combined and uncured 4-AS, IN, and NND waste suspended and/or dissolved in acetone from cleaning beaker with composite from step 3.3.20. Expected amounts of < 5 mL. Some of the uncured 4-AS, IN, and NND can also be considered solid waste.

Section 2: Silicone Mold

2.1 Fabrication of Silicone Rubber Mold

1. Ensure workspace is clear. Gather materials and equipment needed:
   a. Plastic cup or disposable beaker (500 g recommended capacity)
   b. Balance for measurement of materials (minimum 700 g capacity)
   c. Disposable spatula or wooden tongue depressor for mixing
   d. Smooth-Sil 960 Parts A and B
   e. Vacuum pump
   f. Vacuum degassing chamber
   g. Paper towels
2. Zero balance and measure out pre-determined amount of Part A into cup as determined by the size of the 3D-printed antimold.
3. Zero balance again and add the corresponding amount of Part B as determined by the 100A:10B weight ratio set by the manufacturer.

4. Mix with disposable mixing tool until color becomes homogenous (about 3 minutes).
5. Place in degassing chamber.

2.2 Degassing

6. Place lid on degassing chamber and close outlet and inlet valves.
7. Turn on vacuum pump and open inlet valve. Monitor silicone in cup and vacuum pressure. The silicone will begin to bubble and rise to the top of the cup. When the silicone is just below the rim of the cup, close inlet valve and open outlet valve to chamber and allow silicone to come back down to normal level. When the silicone appears back to the starting level, close outlet valve and open inlet valve to continue vacuum. Repeat until silicone no longer bubbles.
8. When no more bubbles appear on the surface of the silicone, close inlet valve, turn off vacuum pump, and open outlet valve to release pressure. Make sure to keep all hands and body parts away from the outlet valve as the vacuum is opened to the environment.

2.3 Antimold and Curing

9. Pour liquid silicone into antimold in a single spot at the lowest point of the antimold and allow it to find its level in the antimold. The liquid silicone should level off at least ½" over the highest part of the antimold surface such that the resulting mold will have a base that is at least ½" thick to provide stability to the mold according to manufacturer's specifications.
10. Once filled, set antimold in isolated space and label accordingly. Cure time is 16 hours.
11. Once cured, gently remove the mold from the antimold and trim as needed.

2.4 Cleaning

Dispose of cup and mixing tool as well as any extra silicone in trash. Ensure vacuum pump and degassing chamber are cleaned and properly stored.

Section 3: Inductor Fabrication

3.1 Preparing Materials for Inductor Fabrication

12. Ensure fume hood and workspace area clear. Gather materials and equipment needed:
    a. Plastic weigh boat (100 g recommended capacity)
    b. Balance for measurement of materials (minimum 200 g capacity)
    c. Vacuum oven moved to fume hood to ensure adequate ventilation during curing
    d. Thermocouples and corresponding measurement tools
    e. Metal spatula for mixing
    f. Toroid mold (see Section 2: Silicone Mold above; maximum working temperature is 232°C)
    g. Heat resistant gloves and tongs
    h. Hot plate (minimum 180°C working temperature)
    i. Thermocouples to measure hot plate temperature
    j. 200 mL beaker

    k. 1000 μL pipette and pipette tip

    l. 50 mL beaker (disposable if possible)

    m. Pre-milled 4-aminophenyl sulfone and iron nitride powder (IN, amount determined by fabrication calculations and provided by sponsor)

    n. N,N-diglycidyl-4-glycidyloxyaniline (NND, amount determined by fabrication calculations)

    o. Vacuum grease

    p. Acetone

    q. Kimwipes

13. Grease silicone rubber mold with a thin layer of vacuum grease and place in oven. Preheat oven (and mold) to 140°C. Ensure thermocouple is in place to accurately measure temperature for data collection and to ensure the mold does not heat beyond its working temperature.

14. Using the balance, weigh boat, and spatula, measure the required amount (as determined by the inductor fabrication calculations) of pre-milled 4-AS and IN into weigh boat. Clean spatula with soap and water and dry completely before using with next material to avoid cross-contamination. Transfer the pre-milled 4-AS and IN to a 200 mL beaker.

15. Pour the required amount of NND into 50 mL beaker to limit contamination with the original container. Using a micropipette and corresponding pipette tip, transfer the required amount of NND to the 200 mL beaker with the milled 4-AS and NND.

3.2 Mixing Materials

16. Transfer 200 mL beaker with milled 4-AS and IN powder and NND viscous liquid to hot plate in fume hood.

17. Don heat resistant gloves before using hot plate. Heat at 180°C for 12 minutes to melt the 4-AS and begin crosslinking the NND polymer.

18. Mix components at above temperature until melted and mixed completely to form a composite, no more than 12 minutes (pot life). Do not remove heat resistant gloves until after composite is transferred to the mold and set to cure in the oven (see section 3.3).

3.3 Mold and Curing

19. Don or keep on heat resistant gloves before handling the mold from the oven.

20. Transfer the composite to the mold either with the mixing spatula or by pouring the composite mixture into the mold. Clean beaker immediately (see instructions below for cleaning beaker used with composite material).

21. Transfer mold with composite to oven at 120°C using heat resistant gloves or tongs. Curing of the composite uses a gradual increase in temperature to 180°C following the thermal recipe below. The gradual increase to cure temperature helps to reduce bubbles in the final composite.

    a. 1 hour at 120°C

    b. 10 minutes at 130°C

    c. 10 minutes at 140°C

    d. 10 minutes at 150°C

      e.   10 minutes at 160°C

      f.   10 minutes at 170°C

      g. At least 12 hours at 180°C (recommend not exceeding 15 hours – the key is to use the same curing time for each sample for consistency)

22. Remove heat resistant gloves once it is safe to do so (when the mold with composite is in the closed oven and the hot plate is turned off and cooling).

23. Once curing is complete, remove mold with composite and air cool in fume hood if not already cooled to room temperature.

24. Once cooled, remove composite from mold and clean mold. Store cured composites in sealed container (plastic box is fine) in designated senior project storage location.

3.4 Cleaning

For all cleaning procedures: Make use of resources efficiently and sparingly.

Weighing out material: clean up space around balance with paper towels and acetone. Dispose of all waste in appropriate waste containers obtained from EH&S as detailed above in Section 1: Hazardous Waste.

Beaker with NND: use acetone to dissolve polymer and pour into labeled liquid waste vessel obtained from EH&S. Ensure beaker is completely clear of polymer before rinsing three times with acetone. Clean beaker with soap and water normally after acetone rinse.

Beaker with composite mixture: it is important to clean this beaker immediately after removing it from the hot plate in step 9 because after the composite cures, it will be extremely difficult to clean. Use acetone and the spatula to loosen the composite from the beaker walls before disposing in the designated waste container as determined by EH&S in Section 1. Use acetone and paper towels if needed. Make sure to rinse with acetone three times before cleaning with soap and water normally.

Mold after curing is complete: clean with dry paper towels to remove vacuum grease before wiping clean with acetone and paper towels. Dispose of solid waste in designated hazardous waste container determined by EH&S in Section 1.

Remove lab coat, gloves, and safety glasses. Wash hands thoroughly.

Appendix C: Toroid Core Masses

Mass of Toroid Prototypes (Mixing)					
Sample Number	**Description**	**During Mixing (g)**	**Post-Curing (g)**	**Mass Loss (g)**	**% Mass Loss**
1	65 vol%, 26 AWG	35.3068	33.5171	1.7897	5.1%
3	65 vol%, 20 AWG	36.7981	35.9875	0.8106	2.2%
2	50 vol%, 26 AWG	29.2948	20.3753	8.9195	30.4%
4	50 vol%, 20 AWG	30.3325	22.6567	7.6758	25.3%

Mass of Toroid Prototypes (Sanding)					
Sample Number	**Description**	**Pre-Sanding (g)**	**Post-Sanding (g)**	**Mass Loss (g)**	**% Mass Loss**
1	65 vol%, 26 AWG	33.5171	30.1496	3.3675	10.0%
3	65 vol%, 20 AWG	35.9875	34.8259	1.1616	3.2%
2	50 vol%, 26 AWG	20.3753	19.1322	1.2431	6.1%
4	50 vol%, 20 AWG	22.6567	21.2026	1.4541	6.4%

Appendix D: Complete Data from COMSOL™ Simulations

65 vol%, 26 AWG Model

Permeability			Electrical Conductivity (S/m)	
10			1.00E-06	
Frequency (kHz)	Inductance (µH)	% Dif Inductance	AC Resistance (Ω)	% Dif AC Resistance
1	246.65	28%	0.67049	13%
10	246.65	29%	0.67058	22%
60	246.65	29%	0.67113	
100	246.65	30%	0.67157	166%
Permeability			Electrical Conductivity (S/m)	
10.12			1.00E-06	
Frequency (kHz)	Inductance (µH)	% Dif Inductance	AC Resistance (Ω)	% Dif AC Resistance
1	249.6	30%	0.67049	13%
10	249.6	30%	0.67058	22%
60	249.6	30%	0.67113	
100	249.6	31%	0.67157	166%
Permeability			Electrical Conductivity (S/m)	
8.1			1.00E-06	
Frequency (kHz)	Inductance (µH)	% Dif Inductance	AC Resistance (Ω)	% Dif AC Resistance
1	199.96	8%	0.67049	13%
10	199.96	8%	0.67058	22%
60	199.96	8%	0.67113	
100	199.96	9%	0.67157	166%
Permeability			Electrical Conductivity (S/m)	
8.1			3000	
Frequency (kHz)	Inductance (µH)	% Dif Inductance	AC Resistance (Ω)	% Dif AC Resistance
1	199.96	8%	0.6711	12%
10	199.96	8%	0.73231	14%
60	199.73	8%	2.8892	
100	199.31	8%	6.8141	7%

Permeability			Electrical Conductivity (S/m)	
8.1			0.20	
Frequency (kHz)	Inductance (µH)	% Dif Inductance	AC Resistance (Ω)	% Dif AC Resistance
1	199.96	8%	0.67027	13%
10	199.96	8%	0.67037	22%
60	199.96	8%	0.67108	
100	199.96	9%	0.6718	166%
Permeability			Electrical Conductivity (S/m)	
10			0.20	
Frequency (kHz)	Inductance (µH)	% Dif Inductance	AC Resistance (Ω)	% Dif AC Resistance
1	246.65	28%	0.67049	13%
10	246.65	29%	0.67065	22%
60	246.65	29%	0.67172	
100	246.65	30%	0.67282	166%
Permeability			Electrical Conductivity (S/m)	
10.12			0.20	
Frequency (kHz)	Inductance (µH)	% Dif Inductance	AC Resistance (Ω)	% Dif AC Resistance
1	249.6	30%	0.67049	13%
10	249.6	30%	0.67065	22%
60	249.6	30%	0.67175	
100	249.6	31%	0.67288	166%
Permeability			Electrical Conductivity (S/m)	
10			3000	
Frequency (kHz)	Inductance (µH)	% Dif Inductance	AC Resistance (Ω)	% Dif AC Resistance
1	246.65	28%	0.67143	12%
10	246.64	29%	0.76471	9%
60	246.2	29%	4.0491	
100	245.41	29%	10.011	31%
Permeability			Electrical Conductivity (S/m)	
10.12			3000	

Frequency (kHz)	Inductance (µH)	% Dif Inductance	AC Resistance (Ω)	% Dif AC Resistance
1	249.6	30%	0.67146	12%
10	249.58	30%	0.76699	9%
60	249.13	30%	4.1304	
100	248.31	30%	10.235	33%

65 vol%, 20 AWG Model

Permeability			Electrical Conductivity (S/m)	
10			1.00E-06	

Frequency (kHz)	Inductance (µH)	% Dif Inductance	AC Resistance (Ω)	% Dif AC Resistance
1	280.95	22%	0.21233	26%
10	280.95	22%	0.21315	91%
60	280.95	24%	0.21772	
100	280.95	26%	0.22137	196%

Permeability			Electrical Conductivity (S/m)	
11.66			1.00E-06	

Frequency (kHz)	Inductance (µH)	% Dif Inductance	AC Resistance (Ω)	% Dif AC Resistance
1	325.69	36%	0.21233	26%
10	325.69	37%	0.21315	91%
60	325.69	39%	0.21772	
100	325.69	40%	0.22137	196%

Permeability			Electrical Conductivity (S/m)	
8.1			1.00E-06	

Frequency (kHz)	Inductance (µH)	% Dif Inductance	AC Resistance (Ω)	% Dif AC Resistance
1	229.73	2%	0.21233	26%
10	229.73	2%	0.21315	91%
60	229.73	4%	0.21772	
100	229.73	6%	0.22137	196%

Permeability			Electrical Conductivity (S/m)	
8.1			3000	

Frequency (kHz)	Inductance (µH)	% Dif Inductance	AC Resistance (Ω)	% Dif AC Resistance
1	229.73	2%	0.21304	25%
10	229.72	2%	0.2867	66%
60	229.43	4%	2.8675	
100	228.9	5%	7.559	98%

Permeability			Electrical Conductivity (S/m)	
8.1			0.20	

Frequency (kHz)	Inductance (µH)	% Dif Inductance	AC Resistance (Ω)	% Dif AC Resistance
1	229.73	2%	0.2123	26%
10	229.73	2%	0.21286	91%
60	229.73	4%	0.21613	
100	229.73	6%	0.21896	196%

Permeability			Electrical Conductivity (S/m)	
10			0.20	

Frequency (kHz)	Inductance (µH)	% Dif Inductance	AC Resistance (Ω)	% Dif AC Resistance
1	280.95	22%	0.21233	26%
10	280.95	22%	0.21316	91%
60	280.95	24%	0.21806	
100	280.95	26%	0.22232	196%

Permeability			Electrical Conductivity (S/m)	
11.66			0.20	

Frequency (kHz)	Inductance (µH)	% Dif Inductance	AC Resistance (Ω)	% Dif AC Resistance
1	325.69	36%	0.21236	26%
10	325.69	37%	0.21348	91%
60	325.69	39%	0.22008	
100	325.69	40%	0.22581	196%

Permeability			Electrical Conductivity (S/m)	
10			3000	

Frequency (kHz)	Inductance (µH)	% Dif Inductance	AC Resistance (Ω)	% Dif AC Resistance
1	280.95	22%	0.21347	25%
10	280.93	22%	0.32571	54%

Frequency (kHz)	Inductance (μH)	% Dif Inductance	AC Resistance (Ω)	% Dif AC Resistance
60	280.39	24%	4.2552	
100	279.4	25%	11.379	64%
Permeability			Electrical Conductivity (S/m)	
11.66			3000	
Frequency (kHz)	Inductance (μH)	% Dif Inductance	AC Resistance (Ω)	% Dif AC Resistance
1	325.69	36%	0.2139	25%
10	325.67	37%	0.36648	43%
60	324.8	38%	5.7032	
100	323.24	39%	15.352	36%

50 vol%, 26 AWG Model

Permeability			Electrical Conductivity (S/m)	
7			1.00E-06	
Frequency (kHz)	Inductance (μH)	% Dif Inductance	AC Resistance (Ω)	% Dif AC Resistance
1	125.07	23%	0.5665	17%
10	125.07	24%	0.56657	20%
60	125.07	24%	0.56692	
100	125.07	24%	0.56721	190%
Permeability			Electrical Conductivity (S/m)	
6.95			1.00E-06	
Frequency (kHz)	Inductance (μH)	% Dif Inductance	AC Resistance (Ω)	% Dif AC Resistance
1	124.18	23%	0.5665	17%
10	124.18	23%	0.56657	20%
60	124.18	24%	0.56692	
100	124.18	24%	0.5672	190%
Permeability			Electrical Conductivity (S/m)	
6.1			1.00E-06	
Frequency (kHz)	Inductance (μH)	% Dif Inductance	AC Resistance (Ω)	% Dif AC Resistance
1	107.56	8%	0.56272	18%
10	107.56	9%	0.56277	20%
60	107.56	9%	0.56304	

Frequency (kHz)	Inductance (µH)	% Dif Inductance	AC Resistance (Ω)	% Dif AC Resistance
100	107.56	9%	0.56325	190%

Permeability			Electrical Conductivity (S/m)	
6.1			3000	

Frequency (kHz)	Inductance (µH)	% Dif Inductance	AC Resistance (Ω)	% Dif AC Resistance
1	107.56	8%	0.5629	18%
10	107.55	9%	0.58081	17%
60	107.52	9%	1.2119	
100	107.45	9%	2.3641	162%

Permeability			Electrical Conductivity (S/m)	
6.1			0.01	

Frequency (kHz)	Inductance (µH)	% Dif Inductance	AC Resistance (Ω)	% Dif AC Resistance
1	107.56	8%	0.56272	18%
10	107.56	9%	0.56277	20%
60	107.56	9%	0.56304	
100	107.56	9%	0.56326	190%

Permeability			Electrical Conductivity (S/m)	
7			0.01	

Frequency (kHz)	Inductance (µH)	% Dif Inductance	AC Resistance (Ω)	% Dif AC Resistance
1	125.07	23%	0.5665	17%
10	125.07	24%	0.56657	20%
60	125.07	24%	0.56693	
100	125.07	24%	0.56722	190%

Permeability			Electrical Conductivity (S/m)	
6.95			0.01	

Frequency (kHz)	Inductance (µH)	% Dif Inductance	AC Resistance (Ω)	% Dif AC Resistance
1	124.18	23%	0.5665	17%
10	124.18	23%	0.56657	20%
60	124.18	24%	0.56692	
100	124.18	24%	0.56721	190%

Permeability			Electrical Conductivity (S/m)	
7			3000	

Frequency (kHz)	Inductance (μH)	% Dif Inductance	AC Resistance (Ω)	% Dif AC Resistance
1	125.07	23%	0.56675	17%
10	125.07	24%	0.59067	16%
60	125.01	24%	1.4341	
100	124.91	24%	2.9731	153%
Permeability			Electrical Conductivity (S/m)	
6.95			3000	
Frequency (kHz)	Inductance (μH)	% Dif Inductance	AC Resistance (Ω)	% Dif AC Resistance
1	124.18	23%	0.56674	17%
10	124.18	23%	0.59033	16%
60	124.13	24%	1.4217	
100	124.03	24%	2.9389	153%

50 vol%, 20 AWG Model

Permeability			Electrical Conductivity (S/m)	
7			1.00E-06	
Frequency (kHz)	Inductance (μH)	% Dif Inductance	AC Resistance (Ω)	% Dif AC Resistance
1	142.01	17%	0.18317	27%
10	142.01	17%	0.1835	50%
60	142.01	18%	0.18536	
100	142.01	20%	0.18685	165%
Permeability			Electrical Conductivity (S/m)	
7.28			1.00E-06	
Frequency (kHz)	Inductance (μH)	% Dif Inductance	AC Resistance (Ω)	% Dif AC Resistance
1	147.31	20%	0.18317	27%
10	147.31	21%	0.18353	50%
60	147.31	22%	0.18553	
100	147.31	23%	0.18713	165%
Permeability			Electrical Conductivity (S/m)	
6.1			1.00E-06	

Frequency (kHz)	Inductance (µH)	% Dif Inductance	AC Resistance (Ω)	% Dif AC Resistance
1	124.99	4%	0.18316	27%
10	124.99	5%	0.18342	50%
60	124.99	6%	0.18486	
100	124.99	7%	0.18601	165%

Permeability			Electrical Conductivity (S/m)	
6.1			3000	

Frequency (kHz)	Inductance (µH)	% Dif Inductance	AC Resistance (Ω)	% Dif AC Resistance
1	124.99	4%	0.18338	27%
10	124.99	5%	0.20488	40%
60	124.94	6%	0.95611	
100	124.86	7%	2.326	18%

Permeability			Electrical Conductivity (S/m)	
6.1			0.01	

Frequency (kHz)	Inductance (µH)	% Dif Inductance	AC Resistance (Ω)	% Dif AC Resistance
1	124.99	4%	0.18316	27%
10	124.99	5%	0.18342	50%
60	124.99	6%	0.18486	
100	124.99	7%	0.18602	165%

Permeability			Electrical Conductivity (S/m)	
7			0.01	

Frequency (kHz)	Inductance (µH)	% Dif Inductance	AC Resistance (Ω)	% Dif AC Resistance
1	142.01	17%	0.18317	27%
10	142.01	17%	0.1835	50%
60	142.01	18%	0.18537	
100	142.01	20%	0.18686	165%

Permeability			Electrical Conductivity (S/m)	
7.28			0.01	

Frequency (kHz)	Inductance (µH)	% Dif Inductance	AC Resistance (Ω)	% Dif AC Resistance
1	147.31	20%	0.18317	27%
10	147.31	21%	0.18353	50%

Frequency (kHz)	Inductance (μH)	% Dif Inductance	AC Resistance (Ω)	% Dif AC Resistance
60	147.31	22%	0.18554	
100	147.31	23%	0.18715	165%
Permeability			Electrical Conductivity (S/m)	
7			3000	
Frequency (kHz)	Inductance (μH)	% Dif Inductance	AC Resistance (Ω)	% Dif AC Resistance
1	142.01	17%	0.18345	27%
10	142.01	17%	0.21176	37%
60	141.94	18%	1.2008	
100	141.81	20%	3.0035	43%
Permeability			Electrical Conductivity (S/m)	
7.28			3000	
Frequency (kHz)	Inductance (μH)	% Dif Inductance	AC Resistance (Ω)	% Dif AC Resistance
1	147.31	20%	0.18348	27%
10	147.31	21%	0.2141	36%
60	147.23	22%	1.2838	
100	147.08	23%	3.2331	50%